CHAPTER IV
RESULTS AND DISCUSSION

4.1 Multiscale molecular simulations of two polymer hosts for gel electrolytes: poly(vinyl chloride) and poly(vinyl fluoride)

This section aims to develop a multiscale molecular simulation to generate and equilibrate amorphous structures of poly(vinyl chloride), PVC, and poly(vinyl fluoride), PVF. Then these models are validated by comparing molecular and material properties results with experimental data.

4.1.1 Conformational Energy

The first part of the method of multiscale molecular simulation is to construct the rotational isomeric state (RIS) model derived from *ab initio* electronic structure calculation which can be used to predict the conformational statistics of PVF, in comparison with PVC. The first step is to determine the conformational energies of the representative molecule for PVC and PVF i.e. 2,4-dichloropentane (DCP) and 2,4-difluororopentane (DFP), respectively, through *ab initio* electronic structure calculations. Figures 4.1 and 4.2 present the description of the first (η and τ) and the second (ω, ω_X and ω_{XX}) order interaction used in the RIS model of PVC and PVF.

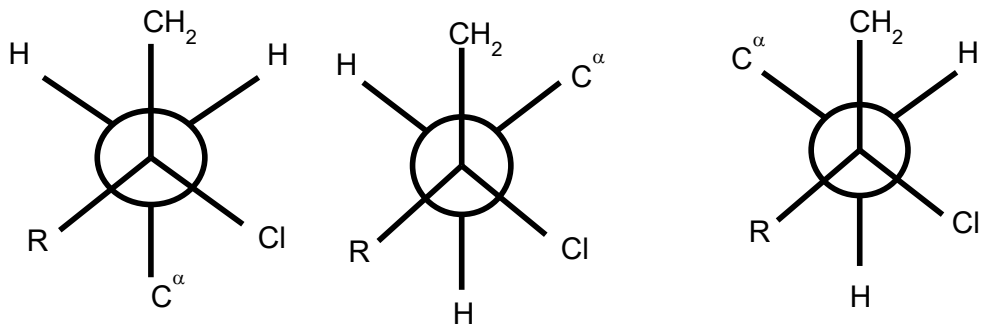

Figure 4.1.1 Newman projections of the *t*, g^+ and g^- conformations of the C-CH_2CH(Cl)-C and C-CH_2CH(F)-C three-bond sequences.

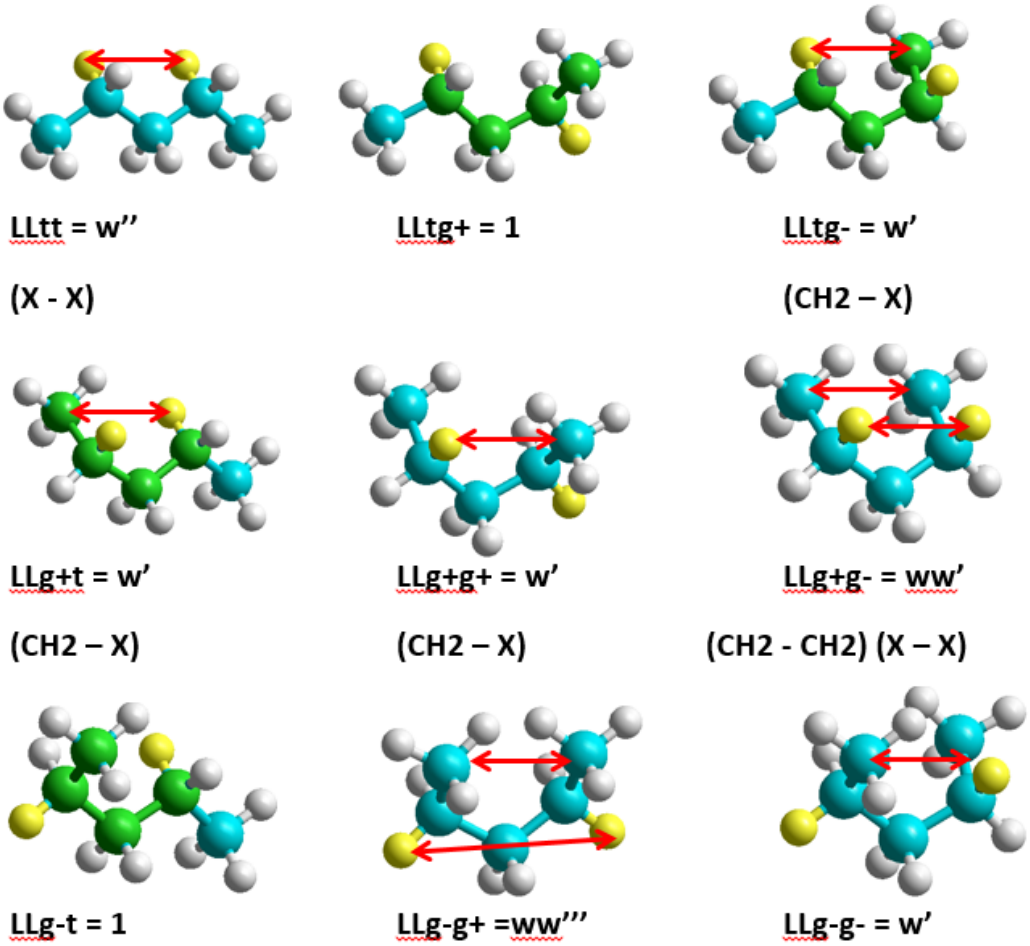

$$D_{ll} = \begin{bmatrix} \omega'' & 1 & \omega' \\ \omega' & \omega' & \omega\omega'' \\ 1 & \omega & \omega' \end{bmatrix} \quad D_{ld} = \begin{bmatrix} 1 & w'' & \omega' \\ \omega'' & \omega'^2 & \omega \\ w' & \omega & 1 \end{bmatrix}$$

Figure 4.1.2 The representative conformation and statistical weight matrices of the second order interaction for PVC and PVC chains with the LL configuration of 2,4-dichloropentane (DCP) and 2,4-difluororopentane (DFP).

In this work, the calculated conformational energies of small molecules, dichloroethance (DCE) and difluoroethance (DFE), based on *ab initio* electronic structure calculation at HF/6-311++G**//MP2/6-311++G** are reported in Table 4.1.1, the conformational energies for DCP, obtained with a 6-311++G** basis set with electron correlation effects considered at the MP2 level, yield a value of E_η = -3.76 kcal/mol and E_η = -1.84 kcal/mol for PVC and PVF, denoting the energy of the racemic *tt* conformer relative to the meso *tg* conformer. In summary, the RIS statistical weight parameters derived from the conformational energy of DCP dimer based on quantum chemistry calculation for PVC are E_η = -3.76 , E_τ, = -2.09 kJ/mol for first-order interaction and E_ω = 7.52, E_{ω_x} = 5.85, $E_{\omega_{xx}}$ = 20.06 kJ/mol for second-order interaction and for PVF are E_η = -1.84, E_τ, = 3.51 kJ/mol for first-order interaction and E_ω = 7.19, E_{ω_x} = 2.51, $E_{\omega_{xx}}$ = 13.63 kJ/mol for second-order interaction. PVF has an unusual small value for E_ω, which is probably due to a small size of the fluorine atom, but $E_{\omega''}$ is large, presumably because it arises in conformations where two C-F dipoles are parallel, and hence interact repulsively. For comparison, various RIS models for PVC and PVF are listed in Table 4.1.2 and Table 4.1.3 including the one from this work.

Table 4.1.1 Conformational energies of 2,4-dichloroethane (DCE) and 2,4-difluoroethane (DFE), (kJ/mol).

DCE and DFE Structures	HF/6-311++G**		MP2/6-311++G**	
	E_{rel} of DCE	E_{rel} of DFE	E_{rel} of DCE	E_{rel} of DFE
LDg$^-$g$^-$	10.847	12.960	7.751	9.899
LDg$^+$g$^-$	20.421	20.277	17.163	17.534
LDtg$^-$	14.419	7.887	12.044	7.004
LDtt	0.000	0.000	0.000	0.000
LDtg+	24.980	17.951	19.683	15.299
LLg$^-$g$^+$	23.208	14.873	21.074	11.717
LLtg$^-$	12.553	7.072	10.000	5.248
LLtg$^+$	4.898	5.976	2.957	4.615
LLtt	23.171	14.530	20.667	13.695

Table 4.1.2 Statistical weights parameter of various RIS models for PVC.

RIS energetics	PVC Flory/Mark[a] (kJ/mol)	PVC Boyd[b] (kJ/mol)	PVC Yoon[c] (kJ/mol)	PVC This work (kJ/mol)
E_η	-3.554	-1.210	-3.766	-4.870
E_τ	1.977	0.790	-2.092	-3.700
E_ω	8.524	10.600	12.552	14.000
$E_{\omega'}$	6.550	6.630	9.623	8.000
$E_{\omega''}$	8.524	9.580	20.083	19.700

[a] Mark, 1972; [b] Boyd, 1981 ; [c] Smith, 1995.

Table 4.1.3 Statistical weights parameter of various RIS models for PVF.

RIS energetics	PVF Saiz[d] (kJ/mol)	PVF Jilin[e] (kJ/mol)	PVF This work (kJ/mol)
E_η	-2.570	-1.841	-1.840
E_τ	-0.613	3.511	-2.761
E_ω	7.220	6.600	6.601
$E_{\omega'}$	1.424	2.514	2.510
$E_{\omega''}$	6.543	13.633	13.634

[d] Carballeira, 1989; [e] Zhang, 2005.

The RIS models with the first- and second-order interactions were constructed based on quantum chemistry calculation and were then employed to calculate the average mean-square unperturbed dimensions of PVC and PVF chains with the probability of *meso diad*, Pm in the range of 0.0 - 1.0. From Figure 4.1.3, the average dimension of PVC chain is more dramatically decreased than that of PVF chain which is slightly decreased as a function of fraction of *meso* diads. The calculation gives results in good consistence with experimental data as shown in Table 4.1.4. The model for PVF predicts C_n to reach 5.0 at ambient temperature for P_m near 0.5. No experimental test of this prediction seems to be available. Both PCF and PVC have E_η < 0 in part because the halogen atom, being smaller than a methyl group, can more easily participate in a *syn* interaction with a methylene group. The value of the energy for this first-order interaction is one of the most differences between the RIS models for PVC by Flory and Williams vs. Boyd and Kesner. The two models predict similar unperturbed dimensions (C_n around 11-12) at ambient temperature for polymers with stereochemical compositions typical of this polymer, P_m = 0.43, in reasonable agreement with experiment. Note that different results are seen between these two proposed RIS models in this work based on AM1 and MP2/6-311++G** calculation with those reported by Mark (1972) and Yoon (1995) for PVC models and Saiz (Carballeira, 1989), Jilin (Zhang, 2005) for PVF models. These findings suggest that it is possible to employ the *ab initio* quantum chemistry calculation to obtain better RIS models to describe the dimension of PVC and PVF chains.

(a)

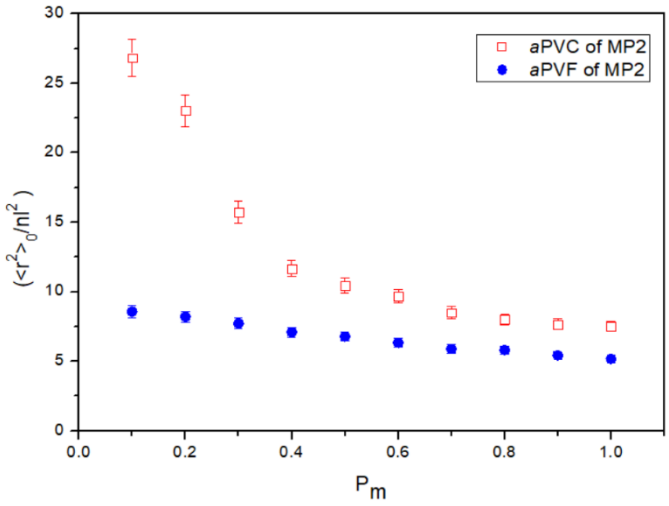

(b)

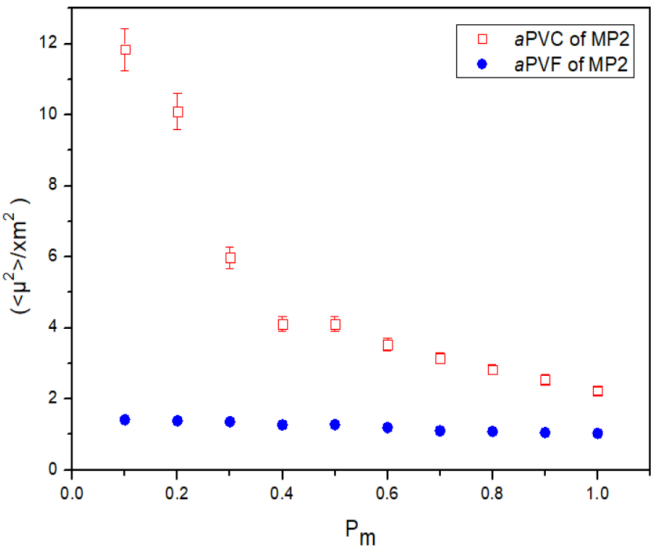

Figure 4.1.3 (a) Characteristics ratio and (b) dipole moment ratio for PVC and PVF chains based on statistical weight matrices determined in this work.

Table 4.1.4 Comparison of the characteristic ratio of PVC and PVF determined by experiment and RIS calculation.

PVC : Characteristic Ratio and dipole moment at 25 °C, (P_m = 0.43)($<r^2>_0/nl^2$)				
Marks	Boyd	AM1	This work	Experiment (P_m = 0.43)
C_n 12.6	10.2	8.7	C_n =11.7	13[a], 8±1[b]
-	-	-	C_m = 4.1	1.4[c] D

PVF : Characteristic Ratio and dipole moment ratio at 323/423 K			
Saiz	Tonelli (50/150°C)	This work	Experiment (P_m = 0.5)
C_n 7.7/6.5	8.1/6.5	C_n = 8.1/6.8	6.0[d]
C_m 1.52/1.37	1.46/1.30	C_m = 1.37/1.28	1.2[d] D

a. Nakajima, 1966; b. Mark, 1972; c. Kivelson, 1960; d. Carballeira, 1989.

4.1.2 Structural relaxation

Equilibration of coarse-grained PVC and PVF at their bulk melts can be justified by the orientation autocorrelation functions (OACF) of the end-to-end vectors, $\left\langle \vec{R}\,(t) \bullet \vec{R}\,(0) \right\rangle$. As presented in Figure 4.1.4(a), chain relaxation can be decayed to zero within 3 x 10^4 and 3 x 10^5 MCS, for PVC and PVF systems, respectively. The decay rate for the rotational motion is faster for PVF than PVC chains about one order of magnitude. For translational motion, the mean-square displacements (MSD) of the chain center-of-mass and at the individual monomer also exhibit similar behavior to the OACF as shown in Figure 4.1.4(b) and 4.1.4(c). For PVF chains, as the intermolecular interaction between CG beads is weaker, their dynamics become faster. In addition, the monomers near chain ends tend to exhibit faster dynamics than those in the inner position. In Figure 4.1.5, the representative snapshots for the coarse-grained models before the reverse-mapping and the fully atomistic structures after energy minimization are illustrated.

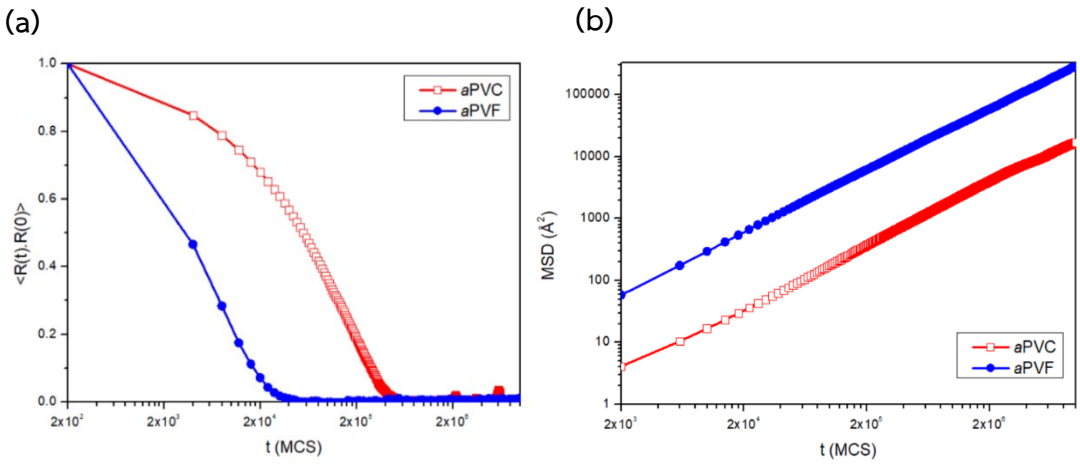

Figure 4.1.4 (a) Orientation autocorrelation function (OACF) of the end-to-end vectors (b) the mean-square displacement (MSD) for the chain center of mass and (c) the MSDs of the individual monomer from MC simulation of bulk PVC and PVF at 600 K.

(c)

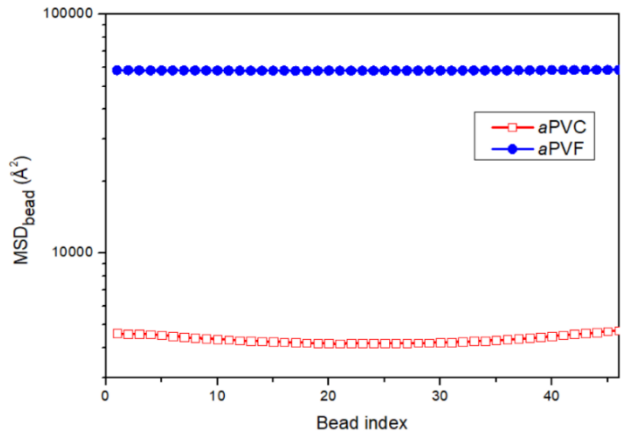

Figure 4.1.4 (a) Orientation autocorrelation function (OACF) of the end-to-end vectors (b) the mean-square displacement (MSD) for the chain center of mass and (c) the MSDs of the individual monomer from MC simulation of bulk PVC and PVF at 600 K (continued).

*a*PVC

*a*PVF

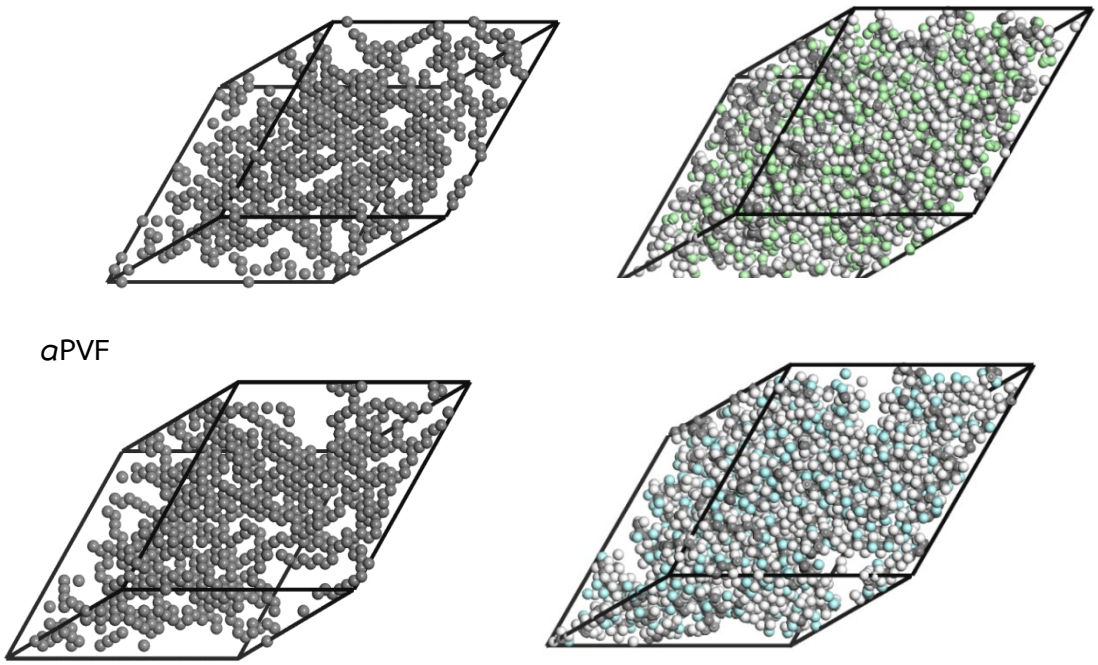

Figure 4.1.5 Example of the snapshot of coarse-grained and fully atomistic models of atactic PVC (above) and PVF (below) at their bulk densities.

4.1.3 Molecular dimension

The mean square radius of gyration ($< R_g^2 >$), the mean square radius of end-to-end distance ($< R^2 >$) and the characteristic ratio ($C_n = < R^2 > / nl^2$) for PVC and PVF chains are presented in Table 4.1.5. The $<R^2>/<R_g^2>$ ratio both for PVC and PVF chains are close to 6.0 in consistent with the theoretical random flight model at long-chain limit (Flory, 1969; Mattice, 1994). Reported experimental results and RIS calculation at the probability of *meso* diads = 0.5 in the long chain limit give the characteristic ratio (C_n) of 13.0 for *a*PVC (Nakajima, 1966) and 6.0 for *a*PVF (Carballeira, 1989). As this simulation is based on relatively short chains (*n* = 46 monomers), smaller magnitudes of C_n are expected. Molecular dimension ($< R_g^2 >$ and $< R^2 >$) and the chain stiffness (C_n) tend to be larger for *a*PVC than those of *a*PVF. However, their magnitudes are within the range of large standard deviation which may not be statistically different. For chain dynamics, the diffusion coefficient for *a*PVF is significantly larger than *a*PVC. Thus, both intramolecular (molecular dimension) and intermolecular interaction should be possible factors to govern the chain dynamics such that PVC exhibit slower dynamics because of larger chain dimension and stronger intermolecular interaction.

Table 4.1.5 Molecular dimension and chain mobility.

Chain	$< R^2 >$ (nm^2)	$< R_{g2} >$ (nm^2)	$< R^2 > / < R_g^2 >$	C_n	D (nm^2 /10^7MCS)	Relative D
*a*PVC	9.21±6.77	1.58±0.68	5.84	4.37±3.20	2.84E-03	0.06
*a*PVF	9.09±6.65	1.50±0.63	6.07	4.31±3.15	4.93E-02	1.00

4.1.4 Conformational statistics

Figure 4.1.6 presents the torsional angle distribution of backbone C-C bonds before and after energy minimization in the conformational states at g^+(60°), *t* (180°) and g^- (300°). During geometry optimization, these torsional angles can be displaced from the lattice sites and the distribution of conformational states becomes continuous in three different kinds of dihedral angles along the backbone as presented in Figure 4.1.6 for both CG and fully atomistic models. The statistics for each conformation state determined from the integral areas of the fully

atomistic model are presented in Table 4.1.6 together with results from the RIS *a-priori probabilities*.

The conformation of atomistic models of *a*PVC and *a*PVF generated by this multiscale simulation are almost equally distributed in the g^+ and g^- state, while the RIS model gives the fraction of g^+ conformation substantially larger than g^- state. This finding may be related to the non-bonded interaction of fluorine/chlorine atoms which are not explicitly included in the RIS model. Due to the smaller size of fluorine atoms, the repulsion occurring at the *gauche* conformation is weaker than that of the chlorine atoms in PVC, thus the *trans* fraction becomes larger with a lower amount of the *gauche* fraction for the PVF chain.

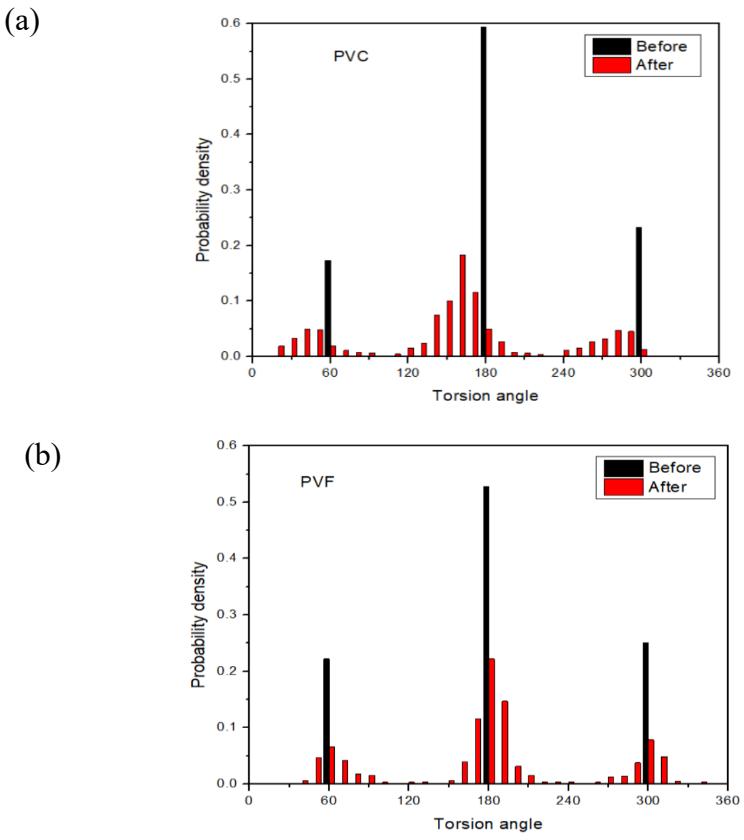

Figure 4.1.6 Distribution of the backbone torsional angles for amorphous (a) *a*PVC and (b) *a*PVF bulks from the reverse-mapping structures before and after energy minimization.

Table 4.1.6 Torsional angle distribution of PVC and PVF models.

Tacticity of polymer chains	Coarse-grained model (MC simulation)			Fully atomistic model (before/after minimization)		
	g^+	t	g^-	g^+	t	g^-
*a*PVC	0.19	0.60	0.19	0.17/0.20	0.59/0.61	0.23/0.19
*a*PVF	0.24	0.53	0.24	0.22/0.23	0.53/0.52	0.25/0.25

4.1.5 Cohesive energy and solubility parameter

One manner to rectify the simulated structures is to compare the calculated cohesive energy and solubility parameters with experimental data. The cohesive energy can be assigned from the energy difference between polymer molecules in the bulk compared to their isolated state. The Hildebrand solubility parameter (δ) can be determined from the cohesive energy density (CED) as (Theodorou, 1985):

$$\delta = (CED)^{1/2} = \left[\frac{\Delta E_v}{V_1}\right] \quad (4.1.1)$$

where V_1 is the molar volume and ΔE_v is equivalent to the cohesive energy, U_{coh} and equal to the difference of the total energy of the bulk structures (U_{tot}) with the parent chains with no periodic boundary condition (U_{par}). The experimental solubilities of *a*PVC and *a*PVF are around 19.2 - 22.1 and 14.6 - 16.3 $J^{1/2}/cm^{3/2}$ (Brandrup, 2004). The calculated cohesive energies are (2.41 x 10^8) ± (2.23 x 10^5) and (1.32 x 10^8) ± (3.76 x 10^5) J/cm^3. The calculated solubility of fully atomistic *a*PVC and *a*PVF models are 15.54 ± 0.0070 and 11.49 ± 0.016 $J^{1/2}/cm^{3/2}$ which are close to the experimental data. Simulation data have high level of confidence as the standard deviations are of small magnitude, the atomistic structure of the amorphous model should be reasonable to represent the real system. The calculated solubility of *a*PVC is larger than *a*PVF implying the more cohesive structure due to the attractive interaction due to chlorine atoms and larger magnitude of dipole moment for C-Cl bonds. Note that the calculated solubility parameter is generally governed by the optimized structure

of the polymer model and the quality of the forcefield used in the calculation, especially the non-bonded interaction terms.

4.1.6 Coarse-grained structures

The pair correlation function (PCFs), $g_{AA}(i)$ of coarse-grained polymer models can be determined from the probability to find the *A* bead from another *A* bead at a distance *r.* For lattice simulation, $g_{AA}(i)$ at the *i*th shell can be defined as:

$$g_{AA}(i) = \frac{1}{(10i^2+2)V_A n_s}\sum n_{AA}(i), \tag{4.1.2}$$

where V_A is the volume fraction of A beads, n_s is the number of structures, and $n_{AA}(i)$ is the number of A beads in the *i*th shell from another A in different chains. At higher shell, $g_{AA}(i)$ approaches 1 for random arrangement. Figure 4.1.7 presents the local intermolecular PCFs.

Since in the first three shells of the non-bond intermolecular interaction parameter for PVC and PVF systems at the simulated temperatures (600 K) are (28.461, 2.547, -1.325 kJ/mol) and (17.369, 0.330, and -0.776 kJ/mol) , respectively. The PCFs are quite small (the magnitude < 1.0) in the first two shells due to the repulsive interaction of non-bonded energy parameters. The first maximum at the third shell is due to the attractive interaction. Interestingly, the magnitudes of PCFs for PVF tend to be larger than those of PVC system at all shells indicating the better packed structure probably due to smaller size of fluorine atom and weaker intermolecular interaction.

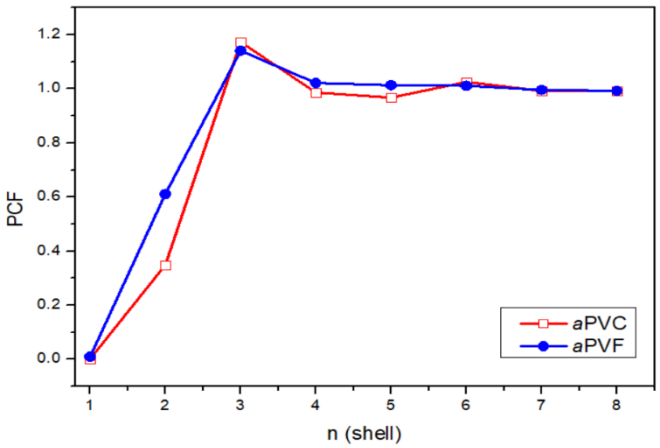

Figure 4.1.7 The intermolecular pair correlation function from MC simulation of the coarse-grained PVC and PVF bulk structures at 600 K.

4.1.7 Radial distribution function

The radial distribution function (RDF) of fully atomistic systems can be determined using a similar definition to the PCF for coarse-grained models on the lattice but in the continuous space. The relationship of each given atom pair AB is averaged out to calculate the RDF by

$$g_{AB}(r) = \frac{\langle n_{AB}(r) \rangle}{4\pi r^2 \Delta r \rho_{AB}} \tag{4.1.3}$$

where $\langle n_{AB}(r) \rangle$ is the average number of AB atom pairs in the spherical shell between the distance r and $r + \Delta r$ (with shell volume = $4\pi r^2 \Delta r$) and ρ_{AB} is the number density of AB atom pairs. According to this definition, RDF gives the probability of finding the separated atom pairs at the distance r, normalized by the probability for a uniform distribution with equal density. The intermolecular RDF gives information about molecular packing and the atomic distribution in the amorphous structure.

In Figure 4.1.8(a), the total RDF of all carbon pairs is presented along with the intermolecular correlations between methine and methylene carbons in Figure 4.1.8(b). It is necessary to confirm whether the generated structures of fully atomistic models are amorphous. The first and second peaks are seen clearly at r = 6.0 and r = 12.0 Å are due to the atomic pair without bond connectivity. The weaker third peak is around

18.0 Å and then the RDF of PVC approach1.0, followed by PVC : C-C, methine-CI, methylene-CI and CI-CI at 33.4, 32.4, 34.2 and 28.1 Å, respectively. For PVF of RDF also reaches 1.0, followed by C-C, methine-F, methylene-F and F-F at 34.5, 35.2, 37.7 and 34.5 Å. Therefore, overall RDF of both polymers, implying that no long-range order exists beyond this distance and the generated atomistic structure is in the amorphous state. In addition, the intermolecular RDFs for halogen atoms in PVC (Cl...Cl) and PVF (F...F) are presented in Figure 4.1.8(c). Due to stronger interaction, the first peak for Cl...Cl correlation is seen at 4 Å and the second peak with higher amplitude is observed at 8 Å. However, there is no clear sign of RDF peak for F...F correlation in PVF probably due to smaller atomic size and weaker intermolecular interaction. Although the size of fluorine atom is smaller, chlorine atoms seem to stay closer to each other. Thus, the intermolecular interaction between PVC chains should be stronger in consistence of larger magnitude of solubility parameter.

(a)

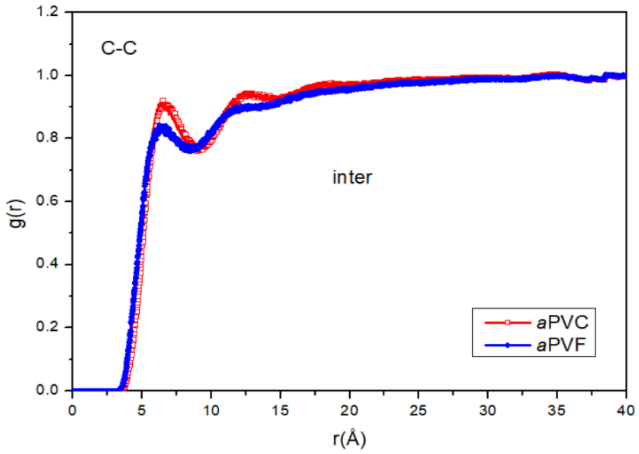

.

Figure 4.1.8 (a) intermolecular RDF of all carbon backbone atoms (b) intermolecular RDF of methine (CH) and methylene (CH_2) carbons and (c) Intermolecular RDFs of Cl...Cl, and F...F atom pairs from the fully atomistic models of amorphous structures.

(b)

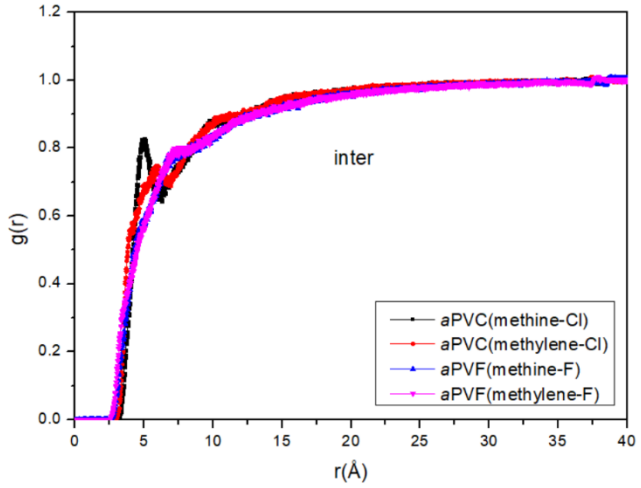

(c)

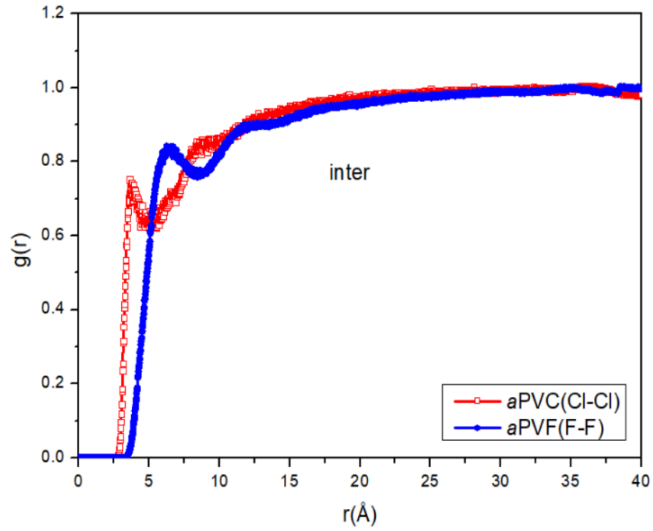

Figure 4.1.8 (a) intermolecular RDF of all carbon backbone atoms (b) intermolecular RDF of methine (CH) and methylene (CH_2) carbons and (c) Intermolecular RDFs of Cl...Cl, and F...F atom pairs from the fully atomistic models of amorphous structures (continued).

4.2 Monte Carlo simulation : Effect of chain stiffness on the free surface of polymers

Because the application of PVC and PVF as the host for gel electrolytes is in the form of polymer surface interacting with ionic liquids, surface properties of these polymers need to be characterized. As seen in the previous section, PVC and PVF have much different chain stiffness in terms of the characteristic ratio. Molecular understanding of surface properties of polymers with different chain stiffness should be important toward material design to give better properties of polymer gel electrolytes to exhibit higher ionic conductivity. Thus, the main aim of this section is to focus on investigation of the effect of chain stiffness on structural and molecular properties of the free surface of polymers. To treat the chain stiffness as the general characteristics, *polyethylene-like* models with varying statistical weight matrices but the same intermolecular interaction parameters are employed to simulate polymers as the free surface.

4.2.1 Equilibration

After coarse-graining PE-like model and mapping onto the 2nnd lattice, the bulk structures were equilibrated using the Monte Carlo algorithm with the single bead move and the acceptance criteria was based on the Metropolis rule. The structures need around 10^7 MCS for equilibration. Data analysis was done from snapshots recorded every 10^4 MCS from the subsequent 10^7 MCS trajectories. System equilibration can be asserted by the mean square displacements (MSD) of polymer chains to exceed their molecular dimension and the normalized orientation autocorrelation functions of the chain end-to-end vector (OACF) < 1/e. As seen in Figure 4.2.1, the equilibration of all structures should be satisfied within 10^7 MCS for the chain stiffness parameters in the range of $0.0 < k < 2.0$. In addition, the local dynamics of monomer units can be represented by the MSDs of individual CG beads. As shown in Figure 4.2.1(c), monomers in the stiffer chains move slower. Moreover, the local dynamics of monomers are increased significantly for CG beads near the chain ends.

(a)

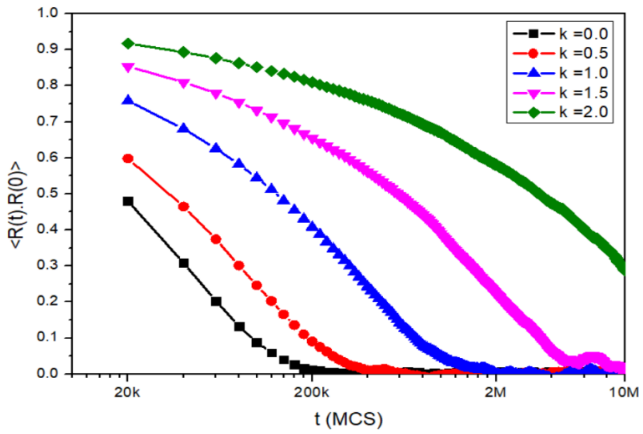

(b)

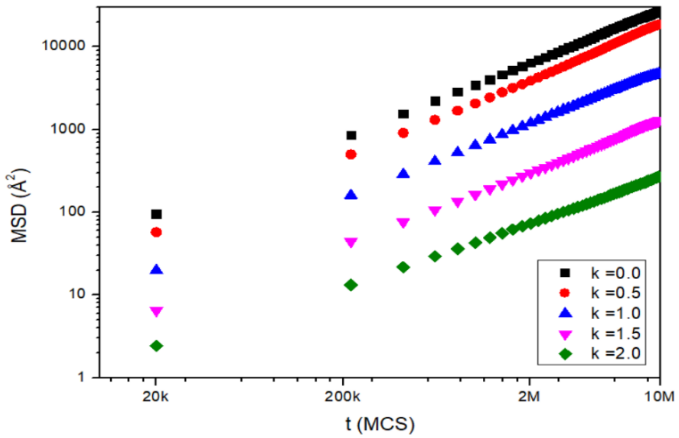

(c)

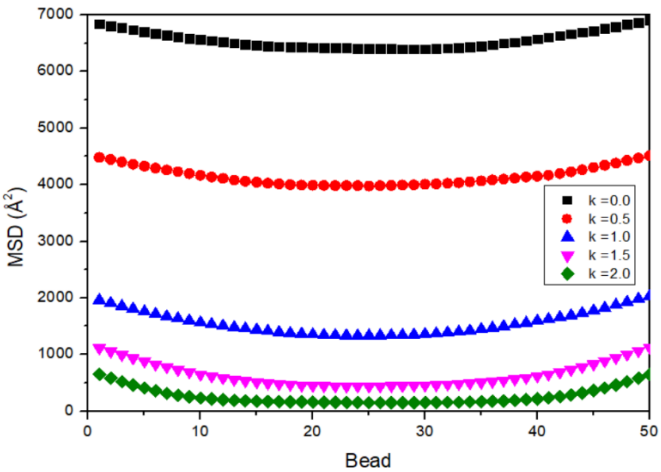

Figure 4.2.1 (a) the OACFs of the chain end-to-end vectors, (b) the MSDs of the chain center of mass, and (c) the MSDs of the individual monomer of polyethylene-like models.

4.2.2 Density profiles

Figure 4.2.2 illustrates the representative snapshots for the free surfaces of polyethylene-like models with different chain stiffness parameters (*k*). In this work, more flexible, normal and more rigid chains are represented by *k* = 0.0, 1.0 and 2.0, respectively. By visual inspection and data for chain conformation in Table 3.2.1, polymers have a larger amount of *gauche* conformation and become denser structures for more flexible chains. In contrast, more rigid chains adopt more *trans* conformation, and the overall structures become less densely packed, especially at the surface where some chains can be exposed more to the vacuum side. The roughness of the free surface in a specific snapshot is defined as $R = (\langle z_p^2 \rangle - \langle z_p \rangle^2)^{1/2}$, where the averages of z_p and z^2_p are taken over all x and y lattice sites across the periodic surface. At any x and y sites, z_p indicates the z coordinate (an integer number) of the outermost bead position of the free surface from the vacuum side. The $\langle R \rangle$ values in Table 4.2.1 indicate the averages over different snapshots separated by 100,000 MCS. The roughness of the free surfaces generally increases when the stiffness parameter is higher. Thus, the broadening of the surface regions observed in the density profiles is also a result of the increased surface roughness.

Density profiles were calculated by counting monomer beads in each divided layer with a thickness of 0.2 nm and then averaged for all trajectories versus the displacement from the center of film structures (Z). Figure 4.2.3 displays density profiles of melt-vacuum surfaces of polymers with different chain stiffness. In general, bulk densities are relatively constant and then sharply decayed near the surfaces. For more flexible chains, there is a larger amount of *gauche* conformation with denser structures. As a result, the bulk densities become higher accompanied by narrower surface thickness.

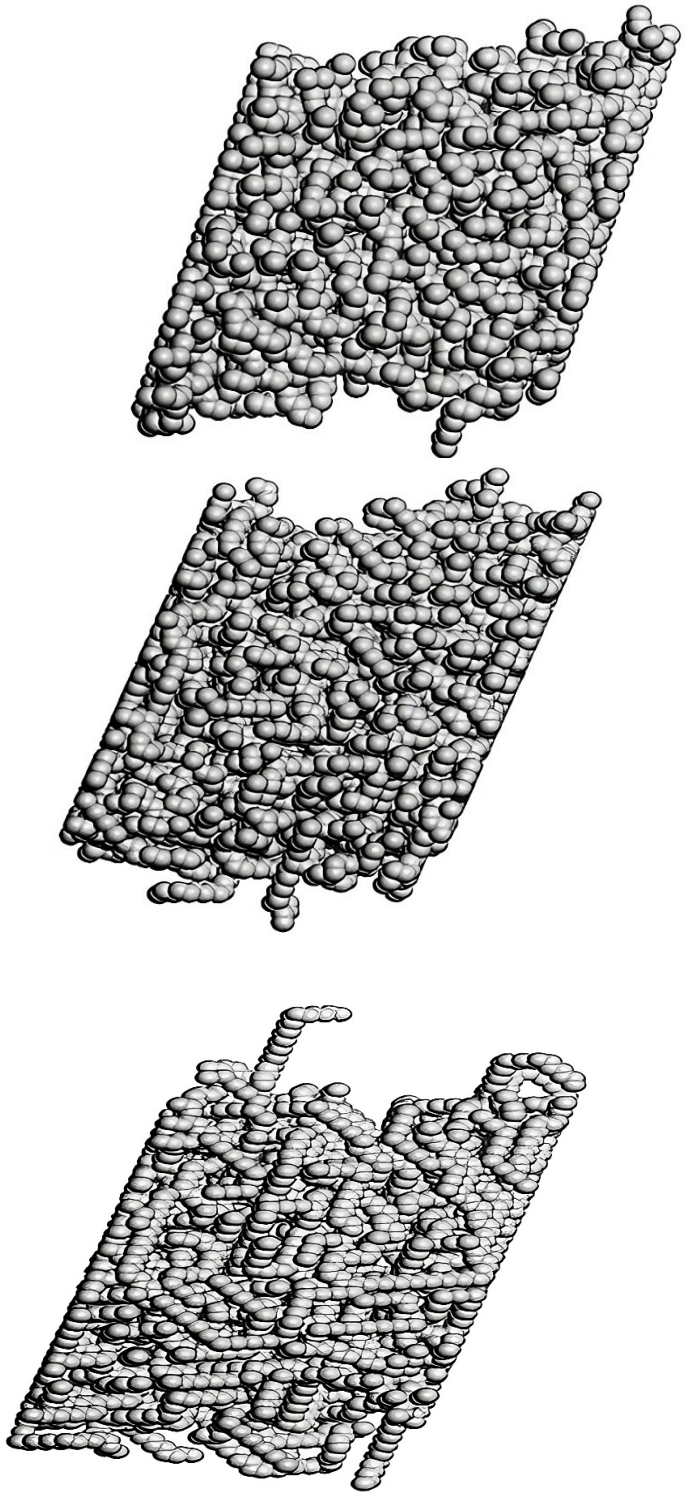

Figure 4.2.2 Representative structures of the free surfaces of polymer melt with different degrees of chain stiffness, k = 0.0 (top), 1.0 (middle), and 2.0 (bottom).

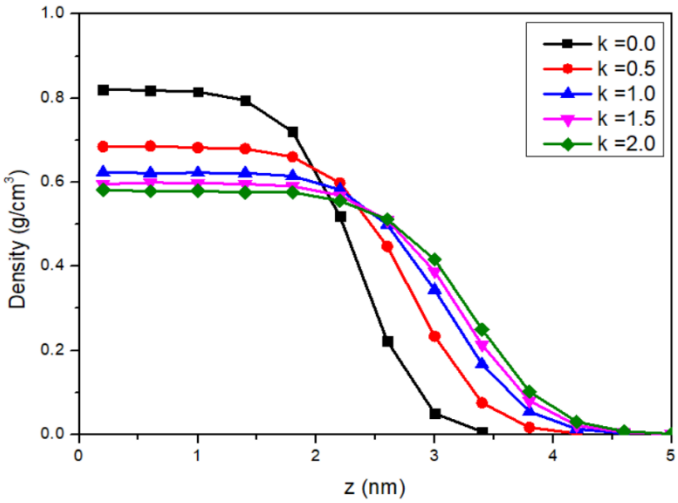

Figure 4.2.3 Density profiles of melt-vacuum surfaces of polymer with different chain stiffness as a function of the displacement from the center of structures.

Table 4.2.1 Parameters of Polymer Surfaces.

Chain stiffness parameter (*k*)	Surface roughness parameter (<*R*>) in lattice units	Bulk density (ρ_{bulk}) g/cm^3	Gibbs surface (z) nm	Surface thickness (*t*) nm	Surface width (w) nm
0.0	4.15 $\pm$ 0.55	0.819	2.336	6.781	1.058
0.5	4.46 $\pm$ 0.60	0.686	2.787	7.885	1.226
1.0	5.74 $\pm$ 0.39	0.625	3.058	8.654	1.336
1.5	6.06 $\pm$ 0.41	0.607	3.968	8.783	1.353
2.0	6.67 $\pm$ 0.47	0.600	4.017	8.938	1.405

*Surface thickness (*t*) is defined as $t = 2z_{1\%}$ where $z_{1\%}$ is the normal distance of the films at 1% of the ρ_{bulk} and is provided as a characteristic size to represent the outer boundary of the films.

To quantitatively analyze polymer surfaces and their relation to the chain stiffness, the theoretical equation originally proposed to describe the interface of immiscible blends is applied (Helfand, 1972).

$$\rho(Z) = \frac{\rho_{bulk}}{2}\left[1 - tanh\left[\frac{2(Z-z)}{w}\right]\right] \qquad (4.2.1)$$

where ρ_{bulk} is the bulk density, Z is the displacement from the center of structures, z is the position where the density is about one-half of bulk density and w is the surface width. The density profiles for these polymer surfaces can be captured very well by this functional form and the fitting parameters are presented in Table 4.2.1. In this work, the Gibbs dividing planes are defined from the density profiles and can be estimated at the z position where $\rho = \rho_{bulk}/2$. The surface thicknesses (t) of the different systems can be estimated from $t = 2z_{1\%}$ where $z_{1\%}$ is defined as the normal distance of the surfaces at 1% of ρ_{bulk} (Doruker, 1998). From Table 4.2.1, it is seen that the surface thickness is larger than the chain dimension by about 3 to 5 times the radius of gyration of polymer chains so that each simulated system can have the bulk region with constant density.

The strength of chain stiffness in polymer surfaces can affect the density profiles, bulk densities, and surface thickness. For stiffer chains, the bulk densities are lower as the structures become less densely packed. The bulk densities are relatively constant and increased proportional to the chain stiffness parameter. Consequently, the surface width (w) and the locations of Gibbs dividing planes used to represent the thickness of surface profiles are inversely proportional to the chain stiffness parameter. The surface thickness changes significantly with the chain stiffness. This outcome is commonly an indication of the adjustment in polymer compressibility as a function of chain stiffness and suggests that the surface thickness, as predicted theoretically by the mean-field approach, is directly correlated to the efficacy of the structure to tolerate density fluctuations. Thus, stiffer chains exhibit thicker surface thickness implying that their surface densities should have larger fluctuations.

Apart from the density profiles, the distribution of polymer chains can be determined by the spatial distribution of their chain center of mass. The chain distributions and their cumulative profiles are shown in Figure 4.2.4. The peak for each profile in Figure 4.2.4(a) on the liquid side of the melt-vacuum surface appears at a distance corresponding approximately to the chain dimension. For more flexible polymers (k = 0.0 and 0.5), their magnitudes seem to be higher in the surface region while this distribution has no systematic difference in the bulk region (Z < 1.5 nm), except the most flexible chain exhibits the largest amplitude. Compared to more

flexible chains, stiffer polymers have less efficiency for chain packing. Thus, the surface becomes broader, and chains can stay at larger distances with increasing chain stiffness. The chain distribution can be systematically distinguished for the cumulative distribution as shown in Figure 4.2.4(b). The cumulative profiles at the same Z position are clearly different only for more flexible chains but almost indistinguishable for stiffer chains. The center of mass density is quite small near the surface as chains do not preferably to be confined close to an essentially impenetrable surface and have pancake-like shapes. Similar findings were also reported in Kumar, 1998 for the off-lattice MC simulation of bead-spring homopolymer models.

To compare the distribution of monomers at different positions in chains, the normalized middle- and end-monomer densities are presented in Figure 4.2.5. The monomer density profiles are normalized by the total monomer density in that bin, so that the distribution near the surface can be observed clearly. This is also typical in the sense that the end beads become more abundant closer to the vacuum. In general, both middle- and end-monomer densities have almost equal magnitude in the bulk region. However, near the surface, the end-monomer profiles are increased exponentially whereas the middle-monomer densities are decreased. This outcome is justified as a competition between the enthalpic (preferably not to have any segments to stay on the vacuum side) and the entropic effects (end-monomers in the free surface constitute smaller entropy loss than middle-monomers) (Kumar, 1994). For more flexible chains, both end- and middle-monomer profiles exhibit steeper curves. As more flexible chains can be packed denser with sharper surfaces, the monomer profiles for end- and middle-beads of more flexible chains exhibit steeper curves accordingly. For stiffer chains, the structures become less dense, and end/middle monomers tend to be placed more in the surface/bulk region (but no significant difference for chains with k = 1.0 - 2.0).

(a)

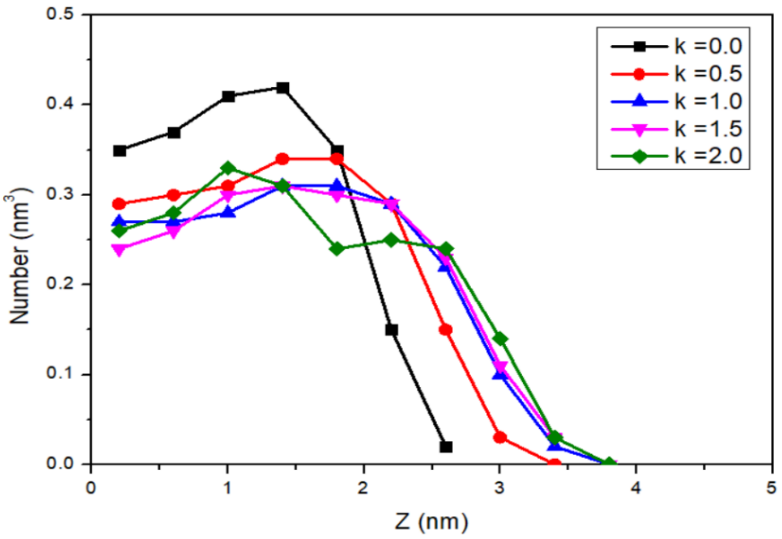

(b)

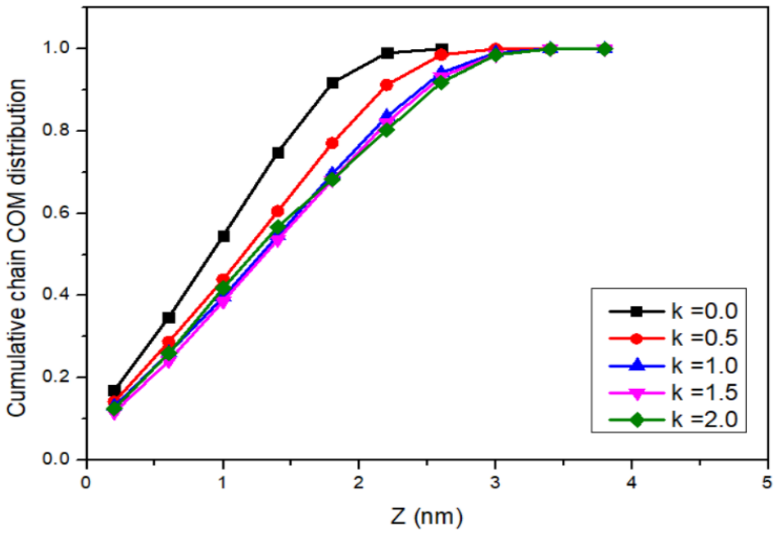

Figure 4.2.4 (a) Distribution of chain center of mass and (b) the corresponding cumulative profiles of polymer surfaces.

(a)

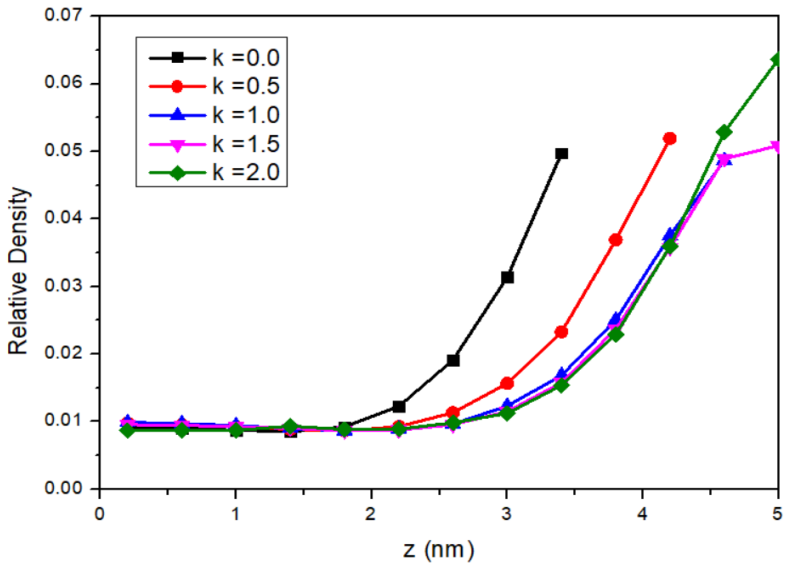

(b)

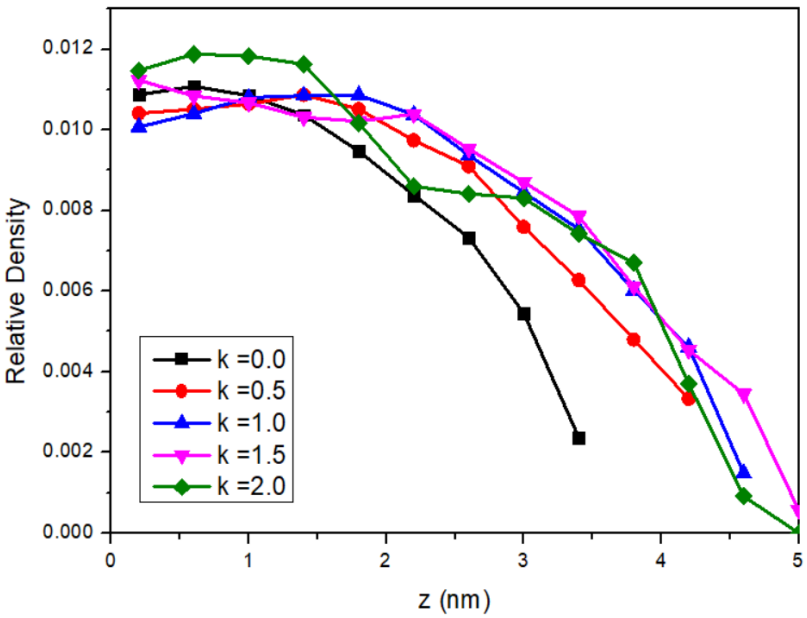

Figure 4.2.5 (a) Relative end-monomer and (b) middle-monomer densities of the free surface of polymer melts at different positions in the structures.

4.2.3 Bond orientation

The bond order parameter (S_b,) is determined to evaluate the orientation of bonds in polymer surfaces as defined by

$$S = \frac{\langle 3\cos^2\theta - 1 \rangle}{2} \qquad (4.2.2)$$

where θ is the angle between a bond vector to the reference vector (the z axis) and <...> is the ensemble average. Thus, bonds tend to have parallel, random, and perpendicular orientations to the surface when S_b = -0.5, 0.0 and 1.0, respectively. As seen in Figure 4.2.6, both middle- and end-bonds exhibit random orientation in the bulk region. However, the opposite behavior is observed near the surface in that the end/middle bonds tend to be aligned in the normal/parallel direction to the surface. For stiffer chains, both end- and middle-bonds tend to have slightly more anisotropic orientation near the surface but no significant difference in the bulk region (except for data at k = 2.0 that chains have a greater fraction of *trans* conformation, especially for the middle-bonds which tend to have more anisotropy).

(a)

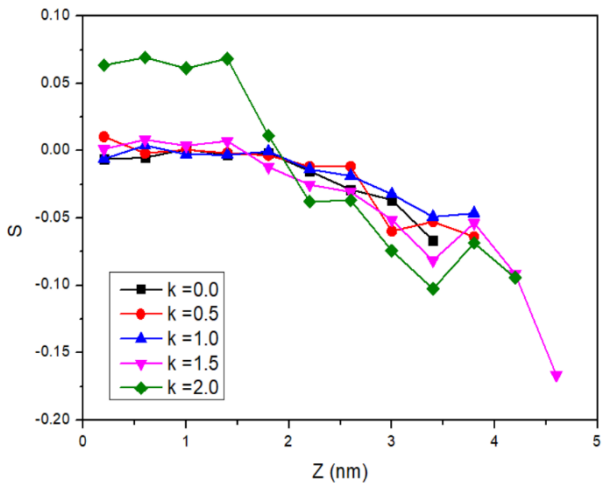

Figure 4.2.6 The order parameter of (a) middle-bonds and (b) end-bonds of the free surface of polymer melts.

(b)

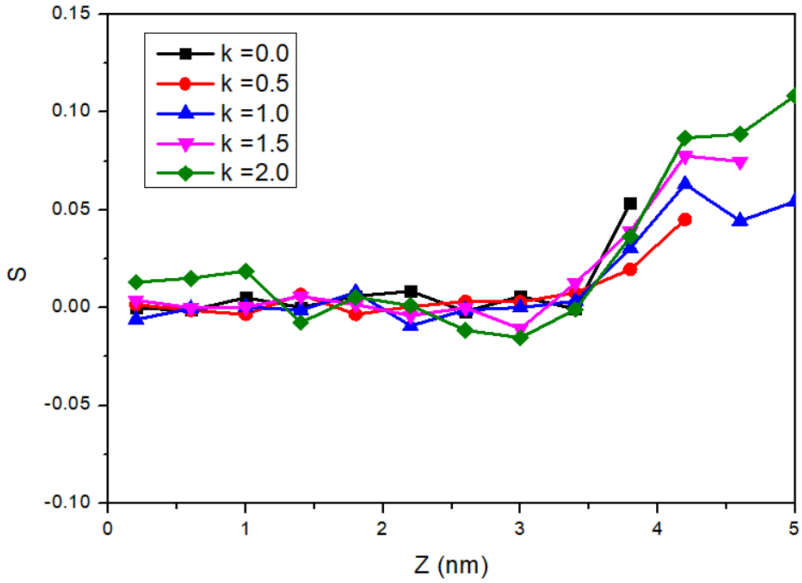

Figure 4.2.6 The order parameter of (a) middle-bonds and (b) end-bonds of the free surface of polymer melts (continued).

4.2.4 Molecular properties

To determine the distortion of molecular dimension for polymers with different degrees of chain stiffness, the mean square end-to-end vector, , $\langle r^2 \rangle^{1/2}$, and the mean square radius of gyration, $\langle s^2 \rangle^{1/2}$ and three principal axes ($L_1 > L_2 > L_3$) derived from the radius of the gyration tensor were calculated and presented in Table 4.2.2. The size of more flexible chains is smaller as the polymer can adopt a greater amount of gauche conformation. As predicted theoretically by the freely jointed chain model at the long chain limit, the $\langle r^2 \rangle / \langle s^2 \rangle$ ratio should be 6.00. Simulation data give larger $\langle r^2 \rangle / \langle s^2 \rangle$ ratio in the range of 6.3 – 6.5 close to the prediction by the RIS model of $\langle r^2 \rangle / \langle s^2 \rangle$= 6.5 for normal polyethylene at the same chain length used in our simulation (Flory, 1969; Mattice, 1994).

In addition, polymer coils can be viewed as an equivalent ellipsoid defined by three principal axes ($L_1 > L_2 > L_3$). According to the freely jointed chain model, the $L_1^2 : L_2^2 : L_3^2$ ratio is theoretically equal to 11.7: 2.7: 1 (Solc, 1971). As presented in Table 4.2.2, the magnitudes of this ratio from the simulation are generally smaller for more flexible chains as they can form a compact shape due to a larger fraction of gauche

conformation. The overall shape of the polymer chain can be evaluated using the definition of acylindricity (c = L_2^2 - L_3^2) and asphericity (b = L_1^2 – (L_2^2+ L_3^2)/2) to represent the deviation from cylindrical (c = 0.0) and spherical shapes (b = 0.0). The acylindricity (asphericity) has noticeably changed from 0.098 (0.465) and 0.046 (0.230) for k = 0.0 and 2.0, respectively. These results suggest that the chain shape is more changed monotonically toward ellipsoid for more flexible chains.

To investigate the anisotropic change in molecular dimension relative to the surface, the XY (parallel) and the Z (perpendicular) components of the mean-squared radius of gyration are determined and depicted in Figure 4.2.7(a) and (b), respectively. The magnitudes of both quantities become larger for stiffer chains where the parallel (perpendicular) components are steadily increased (decreased) and then lower (higher) in the bulk and surface region, respectively. These results are due to chain flattening as polymers are forced to lie near the surface. As a function of the distance from the film center of mass, polymer chains are elongated/shrunk in the parallel/perpendicular direction, respectively, and have pancake-like shapes near the surfaces. The maxima in Figure 4.2.7(a) and the minima in Figure 4.2.7(b) are from the distortion of polymer chains that are confined near an essentially impenetrable surface.

In addition, the change of polymer dimension within the same chain at different positions on the surface can be monitored by the determination of the magnitude of L_1 and L_3 principal axes (normalized by the square radius of gyration). As presented in Figure 4.2.7(c), the magnitudes of both principal axes are larger for more flexible chains as they tend to distort more toward the oblate ellipsoid. The L_1 (L_3) eigenvalues are noticeably decreased (increased) near the surface.

Table 4.2.2 Chain dimension and shape parameters.

Chains	$\langle r^2 \rangle$ (nm^2)	$\langle s^2 \rangle$ (nm^2)	$\langle r^2 \rangle / \langle s^2 \rangle$	$\langle L_1^2 \rangle : \langle L_2^2 \rangle : \langle L_3^2 \rangle$	$\langle c \rangle / \langle s^2 \rangle$	$\langle b \rangle / \langle s^2 \rangle$
k = 0.0	8.29 ± 5.98	1.31 ± 0.54	6.34	9.35:2.59:1.00	0.098	0.465
k = 0.5	9.74 ± 7.13	1.55 ± 0.66	6.25	9.41:2.64:1.00	0.080	0.390
k = 1.0	11.85 ± 8.73	1.87 ± 0.81	6.32	10.15:2.74:1.00	0.066	0.328
k = 1.5	14.46 ± 10.89	2.27 ± 1.01	6.37	11.30:2.90:1.00	0.055	0.275
k = 2.0	17.89 ± 13.34	2.77 ± 1.22	6.46	12.16:3.07:1.00	0.046	0.230

(a)

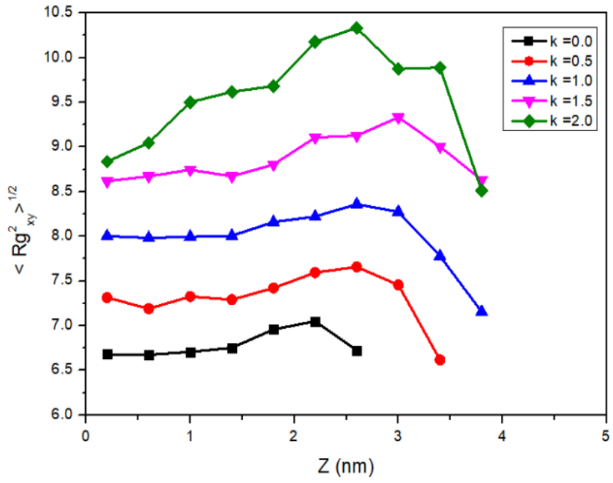

(b)

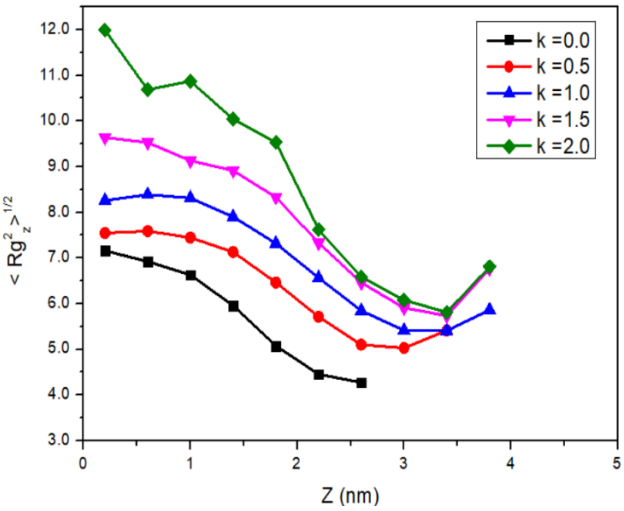

(c)

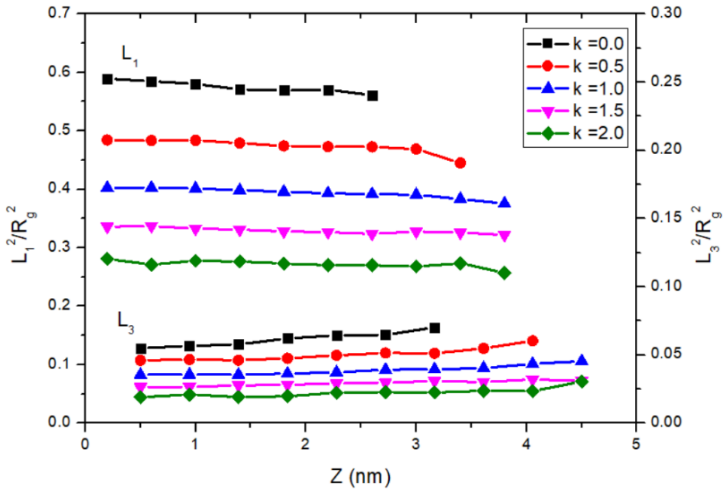

Figure 4.2.7 The components of the mean-squared radius of gyration in (a) the parallel (XY) and (b) the perpendicular (Z) direction to the surface and (c) the first and the third principal axes of polymer molecules.

4.2.5 Molecular orientation

Based on a similar definition to the bond order parameter. The molecular orientation can be evaluated by the calculation for the order parameter of L_1 and L_3 principal axes as the chain vectors. Figure 4.2.8 presents the orientation of L_1 and L_3 vectors relative to the surface. In the bulk region, both molecular axes are randomly oriented (S = 0) for most chains regardless of different degrees of chain stiffness (except for very rigid chains with k = 2.0, which have noticeable anisotropy in parallel orientation to the surface). Toward the surface, the longest vectors tend to be decreased up to Z = 3 nm and then increased after that at the surface. For the shortest vectors, they show random orientation at the distance Z < 3.5 nm and then have anisotropy in the parallel direction at the surface. In addition, the molecular vectors on the vacuum area have negative order parameters with the minimum position near the Gibbs surface. After that, chains can assume more random alignment at the low-density region near the free surface. For polymers with chain stiffness parameters used in this work ($0.0 < k < 2.0$), it seems there is a negligible effect on molecular orientation in these polymer surfaces.

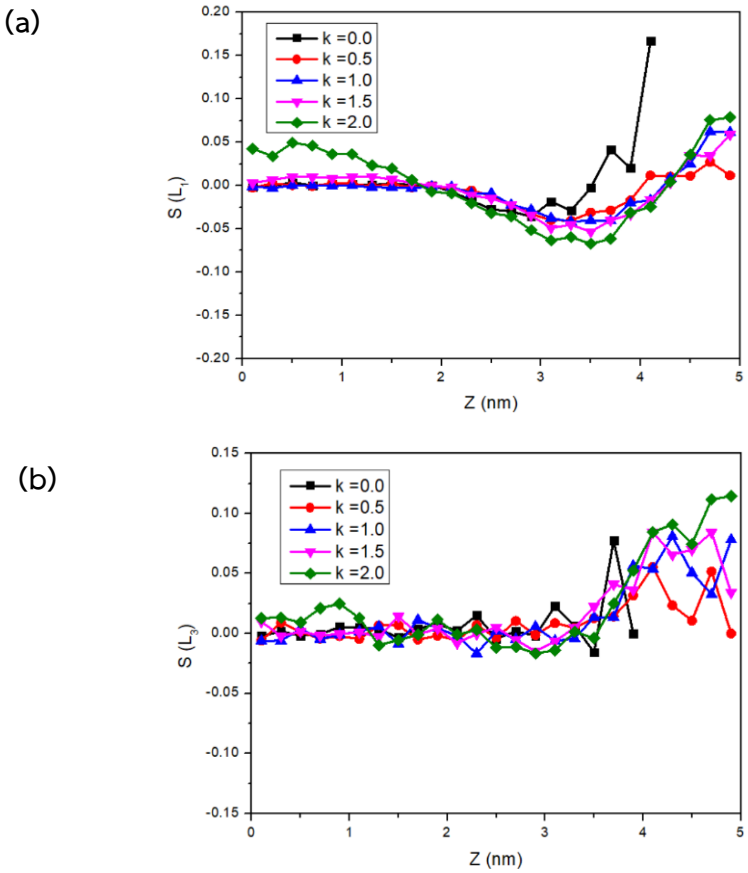

Figure 4.2.8 The chain order parameter of (a) the first and (b) the third principal axes of polymer chains.

4.2.6 Energetics

The intra- and intermolecular energies are presented in Figure 4.2.9 to compare quantitatively the energetics of polymer surfaces. For intramolecular energies in the bulk region, their magnitudes are higher for the more flexible chains due to more *gauche* conformation. In the surface region, intramolecular energies tend to be lower implying that chains have less amount of *gauche* conformation compared to those in the bulk region. For intermolecular energies, their magnitudes in the bulk region tend to be more negative (as the third shell energy is an attractive interaction with a minus sign, u_3 = -0.625 kJ/mol) for more flexible chains which are related to better chain packing. The situation is different in the surface region in that more flexible gain higher intermolecular energies because of the least efficient chain packing.

(a)

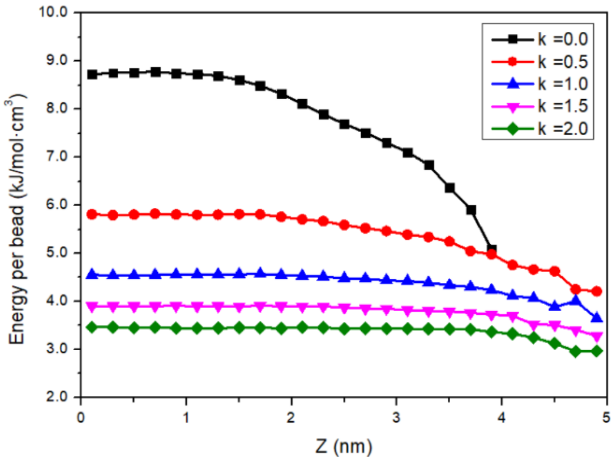

(b)

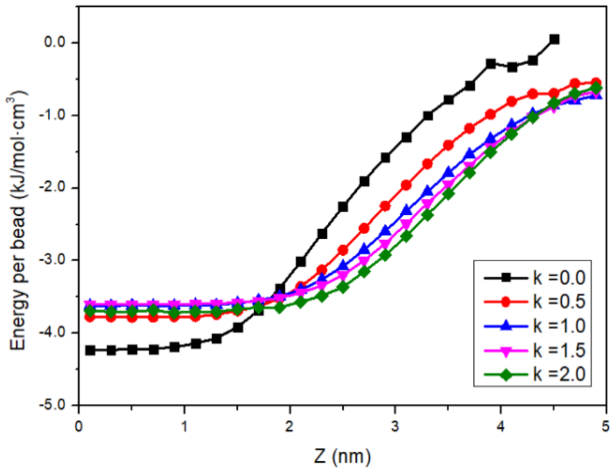

Figure 4.2.9 The profiles of (a) intramolecular and (b) intermolecular energies at different positions in polymer surfaces.

4.3 The effect of intermolecular interaction on polymer crystallization

The ionic conductivity of polymer electrolytes can be related to the ion diffusion in polymer matrices. In general, ions diffuse faster in the amorphous phase. Thus, the ability to control the crystallization characteristics should be important to control the amount of crystalline portion in polymeric materials. One possibility is to add the functional group or modify chain structures to manipulate the intermolecular between chains such as perfluoro-poly(ethylene oxide): -[CH_2CH_2O]- vs -[CF_2CF_2O]- and vinyl polymer -[CH_2CHCl]- vs. -[CH_2CHF]-. Thus, this section will focus on the effect of the intermolecular interaction on polymer crystallization from the molten state investigated by MC simulation. To generalize the effect of different intermolecular interaction, the *PE-like* models were proposed using the same bead dimension (σ = 0.44 nm) but different potential well depth (ε/k = 125 - 205) for more repulsive and more attractive interactions compared to the normal PE chains ($\varepsilon/k = 185$).

4.3.1 Equilibration

Figure 4.3.1 presents the change in the intra- and intermolecular energies for *PE-like* models with different intermolecular interactions at 0-10 million MCS (473 K), 10-20 million MCS (400 K), 20-30 million MCS (350 K) and 30-100 million MCS (298 K). With the same CG bead dimension (σ = 0.44 nm), *PE-like* chains can be considered more attractive (ε/kT >185 K) or more repulsive interaction (ε/kT <185 K) than that of normal PE (ε/kT =185 K). The average values of intramolecular (intermolecular) energies during 50-100 million MCS (298 K) for E125, E145, E165, E185, and E205 are 2760.28+203.90 (-2528.08+44.29), 2132.73+231.70 (-3560.97+55.04), 1891.98+189.44 (-4681.03+50.37), 2155.75+151.38 (-5986.06+52.35) and 2513.75+133.23 (-7130.34+40.28) kJ/mol, respectively. In general, at lower temperatures, chains gain a larger fraction of the *trans* state (see Figure 4.3.4). As the conformational energy of the *trans* state is lower than the *gauche* state, the intramolecular energies become lower. In addition, the intermolecular energies become smaller as polymers can stay closer to other chains. Polymers with more repulsive interaction can have larger intramolecular energies (with larger fluctuation as indicated by the standard deviation) because their bonds tend to adopt more *gauche* conformation (with a higher degree of conformational interconversion).

For polymers with more attractive interaction (E205), chains can have a larger intramolecular energy implying a smaller amount of trans conformation. Note that chains in the E165 system have the lowest intramolecular energy. Thus, chains with a slightly more repulsive interaction than that of normal PE seem to have a larger amount of *trans* conformation. For the intermolecular energies, there is a systematic decrease as a function of intermolecular interaction parameters (ε) implying that the CG beads can stay closer to others for beads with more attractive interaction and the formed structures at lower temperatures tend to be more densely packed.

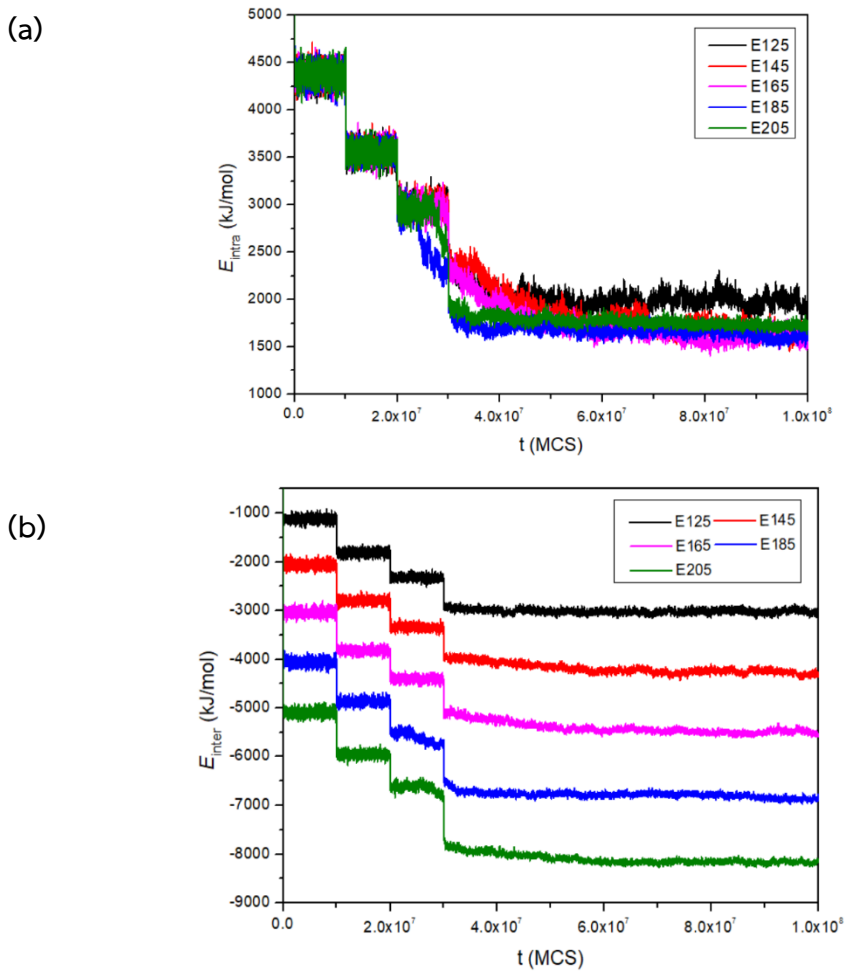

Figure 4.3.1 (a) Intramolecular energies (E_{intra}) and (b) intermolecular energies (E_{inter}), of *PE-like* chains with different intermolecular interactions.

Chain relaxation was determined using the orientational auto-correlation function (OACF) of the normalized end-to-end vector, $<\mathbf{R}(t).\mathbf{R}(0)>/(\mathbf{R}^2)$ and the mean square displacement (MSD) for the chain center of mass, $g_{cm}(t) =< [R_{cm}(t) - R_{cm}(0)]^2 >$ where the end-to-end vector and the center of the mass of chains at time t is denoted by $\mathbf{R}(t)$ and $\mathbf{R}_{cm}(t)$, respectively. As seen in Figure 4.3.2(a), the OACFs at 298 K suggest that the more repulsive chains exhibit faster relaxation in the rotational mode as the structures are less dense with more space for chain reorientation.

For the translational motion, according to the dynamics predicted by the Rouse model for ideal chains, the MSDs should exhibit the Fickian diffusive characteristics ($t^{1.0}$). Usually, the MSDs can show a sub-Fickian regime, t^n (n < 1.0) for $t < \tau_R$ where τ_R is the Rouse time or the relaxation time of the chain end-to-end vector. After that, the MSDs can exhibit the Fickian behavior at longer time. It was reported that MC simulation of CG PE melts on the *2nnd* lattice at 473 K exhibited the Rouse dynamics (Baschnagel, 2000). Here, the dynamics at 298 K for PE-like chains with different intermolecular interactions are explored. From the MSDs data at 298 K shown in Figure 4.3.2(b), the scaling numbers in the sub-Fickian regime and at the long-time limit are proportional to $t^{0.79}/t^{0.74}/t^{0.65}/t^{0.43}/t^{0.30}$ and $t^{0.93}/t^{0.82}/t^{0.75}/t^{0.68}/t^{0.65}$, respectively, for chains in E125/E145/E165/E185/E205 systems. Generally, the scaling numbers are larger for chains with more repulsive interaction. The scaling numbers for all cases are less than 1.0. Thus, the non-Fickian characteristics are observed at both sub-diffusive regimes and the long-time limit at 298 K indicating the effect of intermolecular interaction with their neighboring CG beads.

The monomer dynamics at 298 K can be quantified in terms of the MSDs of individual CG beads as depicted in Figure 4.3.2(c). In general, monomer beads with more repulsive interaction have faster dynamics. Furthermore, the magnitudes of monomer MSDs are increased significantly for the monomers near the chain ends. As discussed previously, this MC method with the current CG polyethylene model gives dynamic characteristics comparable to data obtained from MD simulations of fully atomistic models or experiments with real polymers (Doruker, 1998; Baschnagel, 2000).

Note that chain dynamics are very slow at 298 K because polymers adopt almost all *trans* conformation, and the local chain packing becomes denser. The non-Fickian behavior from the scaling analysis of the MSDs may be caused by the influence of the interaction from nearby chains or a short simulation run with 100 million MCS trajectories. Longer simulation runs should be possible to completely relax the systems, but at the present, it is still impractical based on this MC simulation due to the formidable computational time. Nevertheless, the data presented here are still useful to see the general characteristics of an initial stage of polymer crystallization from the melts.

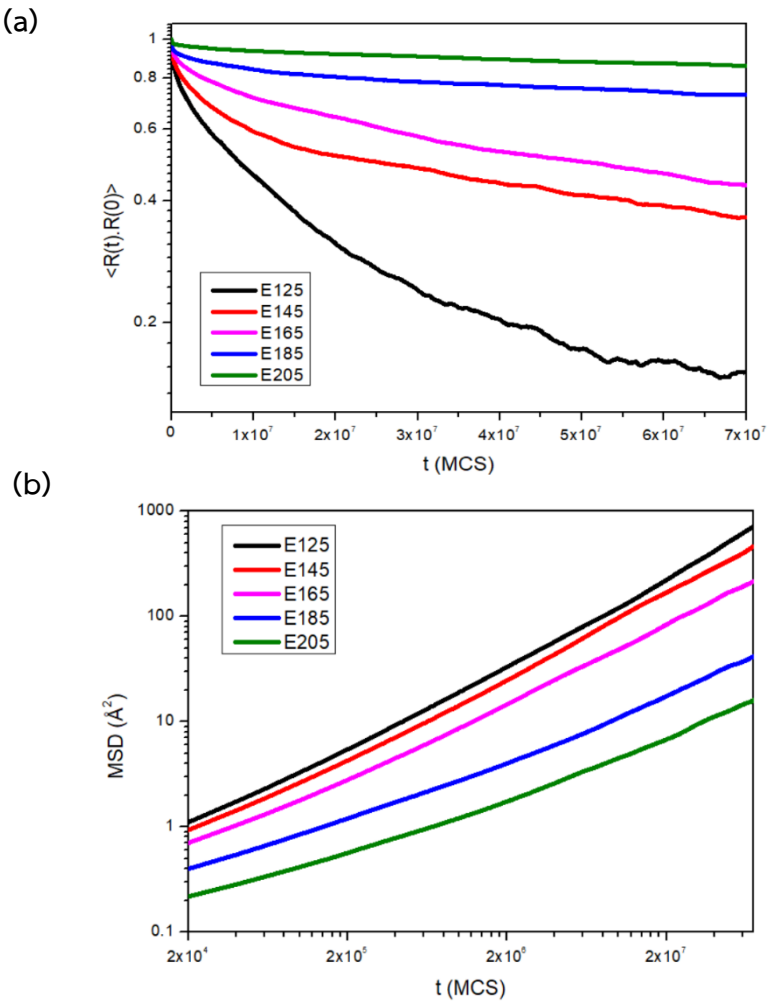

Figure 4.3.2 (a) The OACFs of the chain end-to-end vectors (b) the MSDs of the chain center of mass and (c) the MSDs of individual CG beads of PE-like models with different intermolecular interactions at 298 K.

(c)

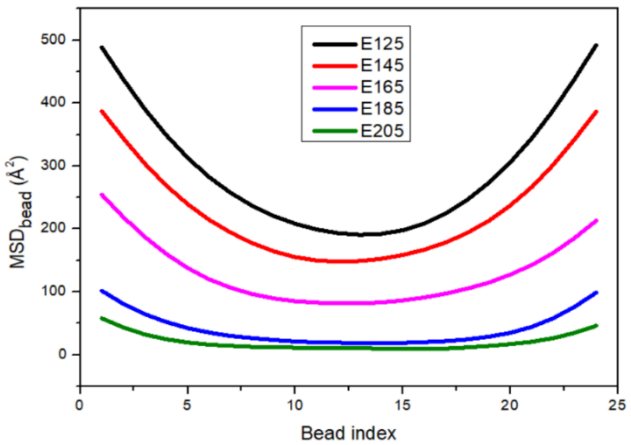

Figure 4.3.2 (a) The OACFs of the chain end-to-end vectors (b) the MSDs of the chain center of mass and (c) the MSDs of individual CG beads of PE-like models with different intermolecular interactions at 298 K (continued).

Figure 4.3.3 presents the final structures at 298 K after 100 million MCS trajectories. Denser structures are seen for chains with more attractive interactions while the less-dense structures are observed for chains with stronger repulsion. When the intermolecular interaction becomes more attractive, chains can be located closer to each other so that the "local packing" with nearby CG beads up to the 8th shell in the *2nnd* lattice becomes denser with the magnitudes of the pair correlation functions (PCF) ordered as E205 > E185 > E165 > E145 > E125 (see Figure 4.3.9). In addition, the averaged values of *trans* fractions and the relative amplitude of chain ordering become lower in cases of too repulsive or too attractive interaction. The fraction of trans conformation and the magnitude of chain order parameters are E145 > E165 >E185 > E205 > E125 (Figure 4.3.4) and E165 > E185 > E145 > E205 > E125 (Figure 4.3.5), respectively. Thus, polymers still have some *gauche* conformation with a lower degree of chain ordering, especially for the most repulsive (ε/k = 125 K) and the most attractive (ε/k = 205 K) interactions.

(a) E = 125

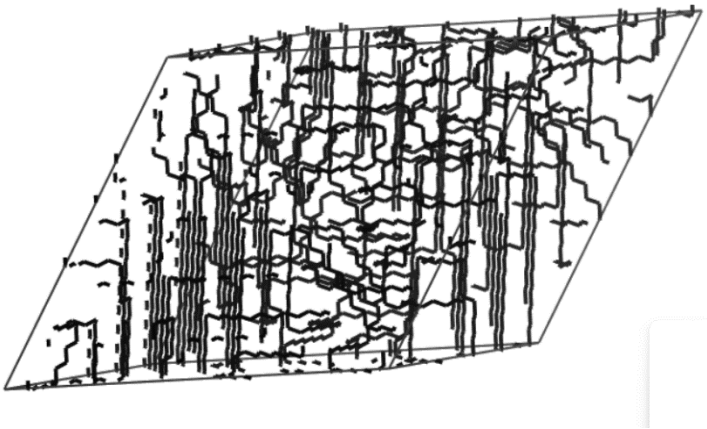

(b) E = 145

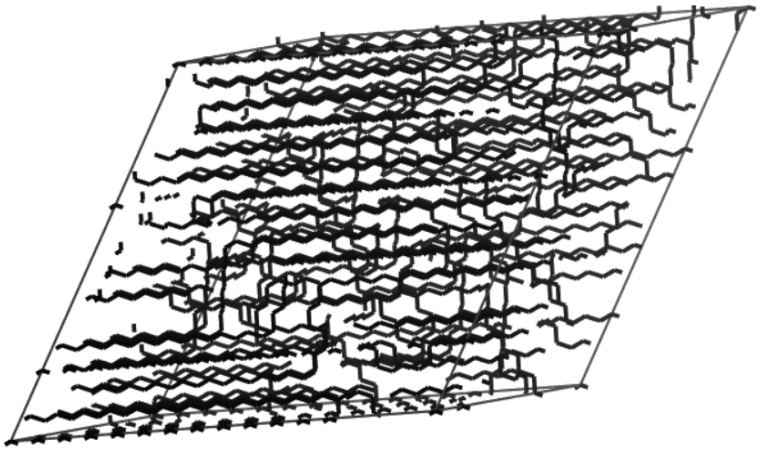

(c) E = 165

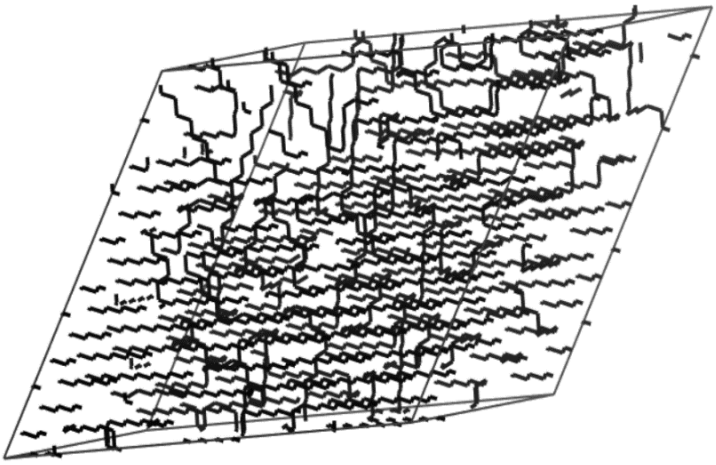

Figure 4.3.3 The final structures after 100 million MCS trajectories at 298 K of PE-like models with different intermolecular interactions (a) E125, (b) E 145 (c) E165 (d) E185 and (d) E205 systems.

(d) E = 185

(e) E = 205

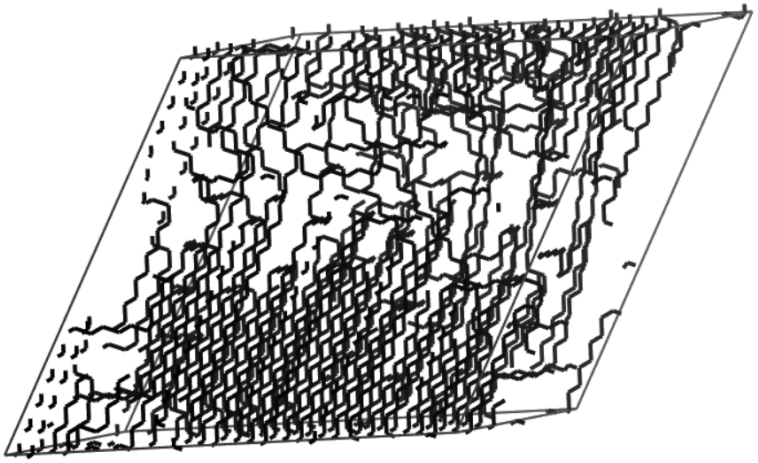

Figure 4.3.3 The final structures after 100 million MCS trajectories at 298 K of PE-like models with different intermolecular interactions (a) E125, (b) E 145 (c) E165 (d) E185 and (d) E205 systems (continued)**.**

4.3.2 Conformation

Figure 4.3.4 presents the *trans* fraction of polymer chains at different temperatures upon cooling from the melts. The smallest magnitudes of the *trans* fractions are seen at 473 K and become higher at lower temperatures. At 298 K (during

50-100 million MCS), the averaged values of the *trans* fractions, are 0.762 ± 0.057, 0.810 ± 0.059, 0.829 ± 0.071, 0.825 ± 0.086, and 0.814 ± 0.081 for chains in E125, E145, E165, E185, and E205 systems, respectively.

Generally, the amplitudes of *trans* fraction tend to be larger for chains with more repulsive interaction except in the E125 system (the most repulsive chains) which exhibits the smallest amount of *trans* fraction than other cases. This is probably because polymers can have more space to interchange the conformation between *trans* and *gauche* states. For chains with more attractive interaction than normal PE, polymer chains in the E205 system can adopt a lower fraction of *trans* conformation. As polymers adopt a larger amount of *gauche* state in the melts (473 K), it should be more difficult for chains with stronger attractive interaction to convert their conformation to the *trans* state at 298 K. Thus, chains with too repulsive and too attractive intermolecular interactions could adopt a lower amount of *trans* conformation at 298 K upon cooling from the melts.

In addition, the magnitude of the *trans* fraction can be increased significantly during 20-30 million MCS (350 K) for chains with different intermolecular interactions in the order of E185 > E205 >E165 > E145 $\geq$ E125. These results show that the normal PE chains have the fastest growth to adopt the *trans* conformation at 350 K followed by chains with slightly more attractive (E205) and slightly more repulsive (E165) intermolecular interaction. Note that even though the normal PE exhibits the fastest growth at 350 K, the final magnitude of the *trans* fraction is not the largest, but it is still smaller than that of the E165 system. Note that there is still a slight increase of the *trans* fraction. Longer simulation at 298 K up to 200 million MCS was also done but the overall results are not significantly different for comparing all systems. Thus, all results reported in this work are based on this 100 million MCS trajectory to focus on the initial stage of structural formation at this temperature.

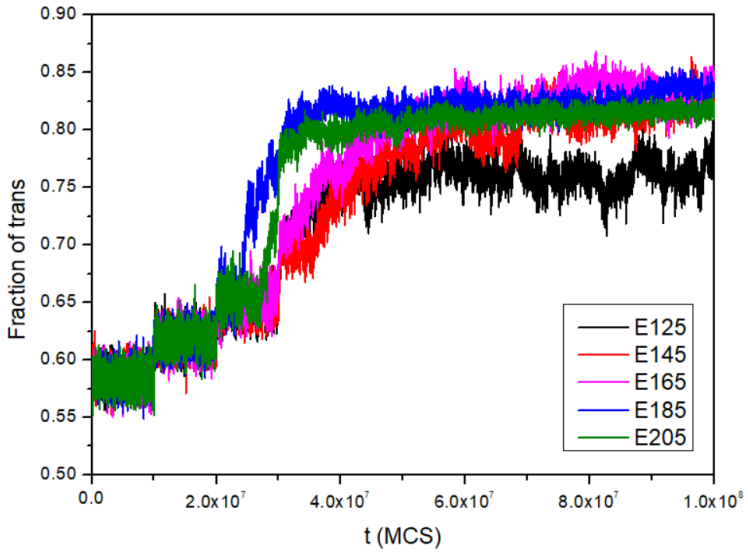

Figure 4.3.4 The fraction of trans conformation of PE-like models with different intermolecular interactions.

4.3.3 Chain dimension

The mean square radius of gyrations,$< R_g^2 >$, is used to represent the chain dimension as presented in Figure 4.3.5. At 400 K and 473 K, the magnitudes of $< R_g^2 >$ are relatively fluctuated around the constant values and become larger for more repulsive chains. Then, $< R_g^2 >$ is increased during 20 - 40 million MCS (at 350 K) in most systems, especially for more attractive chains in E205 with the fastest growth comparable to the normal PE chains. At 298 K, the molecular dimension, averaged during 50-100 MCS, for all the chains can be ordered as E145 $\geq$ E165 > E185 $\geq$ E125 > E205 with the averaged magnitude and the standard deviation of 125.93 $\pm$ 7.22, 136.66 $\pm$ 8.01, 133.40 $\pm$ 7.19, 126.18 $\pm$ 3.45 and 122.94 $\pm$ 2.66 respectively. Except for the E125 systems (the most repulsive chains), the more repulsive chains generally tend to have larger chain dimensions and larger fluctuations. This is because the CG beads tend to stay away from others and polymer chains are more expanded and have more frequent conformational changes. As expected, the more attractive chains (E205 system) have the smallest magnitude of chain dimension and standard deviation as polymers become more compact and get denser structures. Chains with too repulsive

and attractive interactions exhibit smaller chain dimensions because polymers can adopt a larger amount of *gauche* conformation as described in the previous section. Thus, only polymers with the appropriate intermolecular interaction parameters (close to normal PE) can exhibit the largest chain dimension upon stepwise cooling from the molten state.

4.3.4 Chain orientation

To monitor the signal of crystal formation, the overall orientation order parameter of polymer chains, SG, can be calculated according to In this calculation, polymer coils are viewed as the ellipsoid shape with three molecular axes ($L_3 < L_2 < L_1$) obtained from the diagonalization of the radius gyration tensor. The longest (L_1) axis was chosen to determine for chain orientation. Here, the angle (θ) is formed between two L_1 axes from different chains so that the random and parallel orientation can be represented by S_G = 0 and 1, respectively.

$$S_G = \frac{1}{2}[3\langle cos^2\theta \rangle - 1] \quad (4.3.1)$$

In this calculation, polymer coils are viewed as the ellipsoid shape with three molecular axes ($L_3 < L_2 < L_1$) obtained from the diagonalization of the radius gyration tensor. The longest (L_1) axis was chosen to determine for chain orientation. Here, the angle (θ) is formed between two L_1 axes from different chains so that the random and parallel orientation can be represented by S_G = 0 and 1, respectively.

As seen in Figure 4.3.6, S_G for all systems is about zero (random orientation) during the first 20 million MCS (473 and 400 K). Then, S_G for normal PE and slightly more attractive chains (E185 and E205) start to increase during 20-30 million MCS (350K) while chains with more repulsive interaction still assume random orientation but their S_G starts to increase at 298 K. The MCS for chains starting to have more ordered orientation can be arranged as E185 > E205 > E165 = E125 > E145. These results imply that only chains with the appropriated intermolecular interaction close to normal PE can exhibit a faster growth of chain orientation. Slightly attractive chains can draw nearby molecules to induce the ordered orientation even at 350 K. At 298 K, the

magnitudes of S_G averaged during 50-100 million MCS are E125 (0.346 $\pm$ 0.093), E145 (0.677 $\pm$ 0.104), E165 (0.778 $\pm$ 0.061), E185 (0.767 $\pm$ 0.042), E205 (0.553 $\pm$ 0.024).

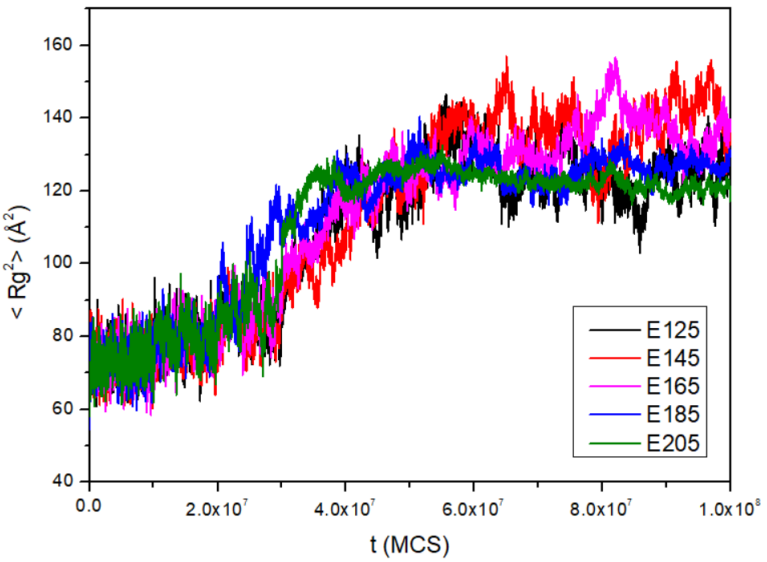

Figure 4.3.5 The mean square radius of gyration of PE-like models with different intermolecular interactions.

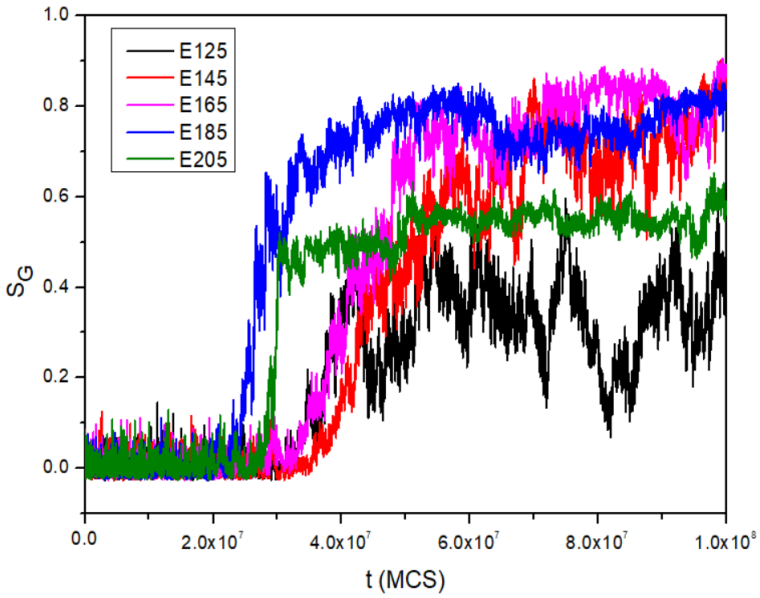

Figure 4.3.6 The global order parameter for *PE-like* models with different intermolecular interactions.

Upon crystallization, PE chains should gain a larger fraction of *trans* state and have a higher degree of intramolecular bond correlation. The first-order intramolecular bond order parameter, $M_1(j)$ can be calculated to evaluate the bond correlation in the same molecule according to

$$M_1(j) = < m_i . m_{i+j} > = < \cos \theta_{i,i+j} > \quad (4.3.2)$$

Here, $\theta_{i,i+j}$ is the angle between (*i+j*)th and (*i*)*th* bonds within the same chain. The characteristics of $M_1(j)$ for intramolecular bonds in the ordered structures formed at 298 K are presented in Figure 4.3.7. Generally, the magnitudes of $M_1(j)$ should be smaller as a function of the bond index (*j*) as polymers adopt a larger amount of the *gauche* state at the further bonds apart. For all systems, $M_1(j)$ reaches 0.0 (disordered) around the 10th bond. For comparison, $M_1(j)$ for chains in E205 dropped to 0.0 at the fastest growth followed by E185 and E125, respectively. Thus, chains with slightly more attractive interaction can have a more disordered intramolecular bond correlation for $j \leq 10$ even though chains with more repulsive interaction in E125 have a larger fraction of *gauche* conformation (see Figure 4.3.4). For bond index $j > 10$, the magnitudes of $M_1(j)$ can be less than 0.0 and can be generally proportional to the strength of intermolecular interaction in the ordered as E205 < E125 < E145 < E165 < E185. Note that the data for E205 has the lowest amplitude at the *j* index around 10 but then exhibits the upturn to have the largest value at $j \geq 16$ with $M_1(j)$ close to zero. These results suggest that intramolecular bonds in E205 exhibit the most disordered orientation due to the attractive interaction between chains.

For chains with more repulsive intermolecular interaction, $M_1(j)$ exhibits monotonically decayed profiles with the magnitude for bond j > 10 closer to 0.0 for more repulsive chains. These findings suggest that the anisotropy of intramolecular bond correlation should be related to the intermolecular interaction between chains and the intramolecular bond orientation becomes more disordered for more repulsive chains at j > 10 bonds. Thus, for chains with too repulsive or attractive interaction, the bonds within the same chains tend to exhibit more disordered orientation in their crystal structures formed under stepwise cooling from the molten state. For chains

with too repulsive interaction, bonds in the same chains can adopt a larger amount of gauche conformation resulting in a lower degree of intramolecular bond correlation. For chains with too attractive interaction, the gauche conformation that occurred in the melt state can not be effectively converted to the trans state. Thus, there is still some amount of gauche conformation which also results in a lower degree of intramolecular bond correlation. The more repulsive chains, the more disordered the orientation for bonds within the same chains.

Next, the intermolecular bond orientation order (S_L) is calculated to determine the bond orientation between different molecules according to

$$S_L(n) = \frac{1}{2}[3 < \cos^2\psi(n) > -1] \quad (4.3.3)$$

where $\psi(n)$ is the angle between two bonds at the reference position and the *n*th shell in the *2nnd* lattice.

Figure 4.3.8 presents the intermolecular bond orientation order for each system at 298 K. Generally, the magnitudes of S_L are near 0.0 in the first shell (bonds tend to be random orientation) due to the most repulsive non-bonded interaction so that the bond can be oriented in any direction. Then bonds show the largest degree of anisotropic arrangement in the second shell (equivalent to the distance at 0.5 nm). For bonds in the further shells, the magnitudes of S_L are monotonically lower implying that intermolecular bond orientation tends to be a more random arrangement at the longer separated distance. The relative magnitudes of S_L in each system can be ordered as: E165 < E185 << E205 < E145 << E125. A large magnitude of S_L (higher degree of intermolecular bond correlation) can be observed for the E185 and E165 systems. Thus, bonds in normal PE and the chains with slightly more repulsive interaction exhibit the highest correlation due to the most ordered structures formed upon stepwise cooling from the melts. Note that for chains with more attractive interaction (E205), intermolecular bond orientation can have a higher correlation than those bonds in more repulsive chains (E205 < E145 << E125). Thus, chains with excessive attractive or repulsive interaction should induce the intermolecular bonds to become more random orientation.

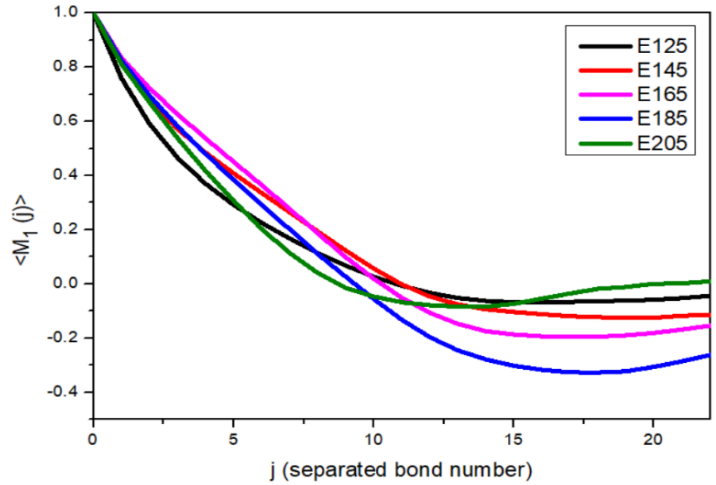

Figure 4.3.7 The intramolecular bond orientation correlation functions for PE-like models with different intermolecular interactions.

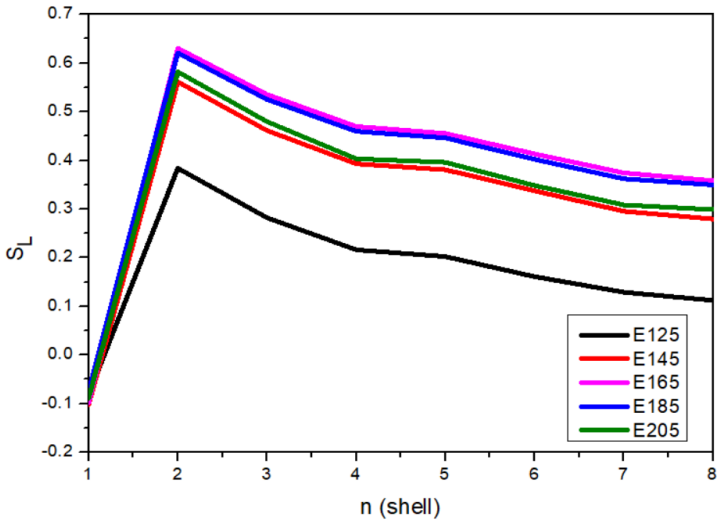

Figure 4.3.8 The correlation function of intermolecular bond orientation for *PE-like* models with different intermolecular interactions.

4.3.5 Structural packing

Structural packing was evaluated in terms of the intermolecular pair correlation function (PCF) calculated from the probability of having two CG beads at different shells on the 2nnd lattice according to

$$g_{AA}(i) = \frac{<n_{AA}(i)>}{(10i^2+2)V_A} \quad (4.3.4)$$

where, $n_{AA}(i)$ is the number of CG beads at the *i*th shell from the reference bead; V_A is the volume fraction of CG beads in *2nnd* lattice (V_A = 0.225). $10i^2$ + 2 is the coordination number of the i^{th} shell. Figure 4.3.9 depicts the PCFs for *PE-like* chains with different intermolecular interactions at 298 K. The PCFs exhibit the maxima in the third shell due to the most attractive interaction of the discretized LJ energies on the *2nnd* lattice. The magnitudes of PCFs tend to be smaller for further shells and have almost the same values after the 7^{th} shell. The magnitudes of PCFs can be generally compared as: E205 > E185 > E165 > E154 > E125. These data suggest that CG beads can stay closer to each other as a function of the intermolecular interaction parameters. For more attractive interaction, the chain packing becomes denser. The trend seen in the PCFs is different from the behavior of the order parameter (S_G) and the amount of *trans* conformation as the PCFs are evaluated at the scale of CG beads. For example, chain properties (order parameter and *trans* fraction) in the more attractive (E205) system can be lower even though the magnitudes of PCFs are higher.

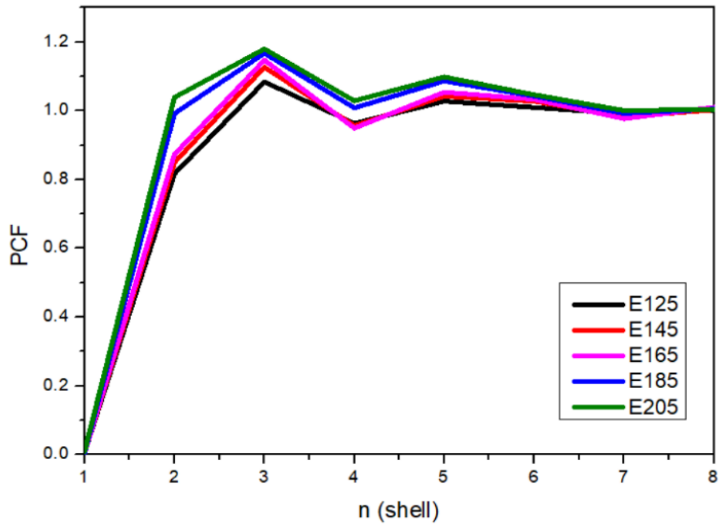

Figure 4.3.9 The intermolecular pair correlation function for the *PE-like* models with different intermolecular interactions.

4.4 Molecular dynamics (MD) simulation of detailed structures and ion transportation of polymerized ionic liquid/ionic liquid blends

This section will mainly focus on both molecular dynamics simulations and experimental studies of polymerized ionic liquids (Pbvim-TFSI) and polymerized ionic liquids-ionic liquids blends (PbvimTFSI-BmimTFSI). Characterizing transport properties of such blends and thereby address the manner by which conductivity can be tuned by the addition of pure ILs to polyILs.

4.4.1 Validated method for equilibration: PolyIL–IL Blends at 600K.

4.4.1.1 Indicating a sufficient structural equilibration for the simulated systems

Equilibration of the polymer systems such as IL, PolyIL and PolyIL-IL blends can be determined by evaluating the potential energy and density. As depicted in Figure 4.4.1 and Figure 4.4.2, after initial setup or after change of parameters, system is out of equilibrium. And its properties will not be stationary, so we are interested in equilibrium, must wait for a number of time steps to reach equilibrium before measuring observables. In most cases, there are two types of checks that the system enters equilibrium as follows: density and radius of gyration is molecular size values. And the reason for not using potential energy determines to enter equilibrium because sometimes the energy is stationary but has not yet reached equilibrium. So that the system reaches its equilibrium, show that no drift in density and the radius of gyration (R_g) of polymer chains were observed. So, the structures in IL, PolyIL and PolyIL-IL blends in Figure 4.4.3 are reached equilibrium..

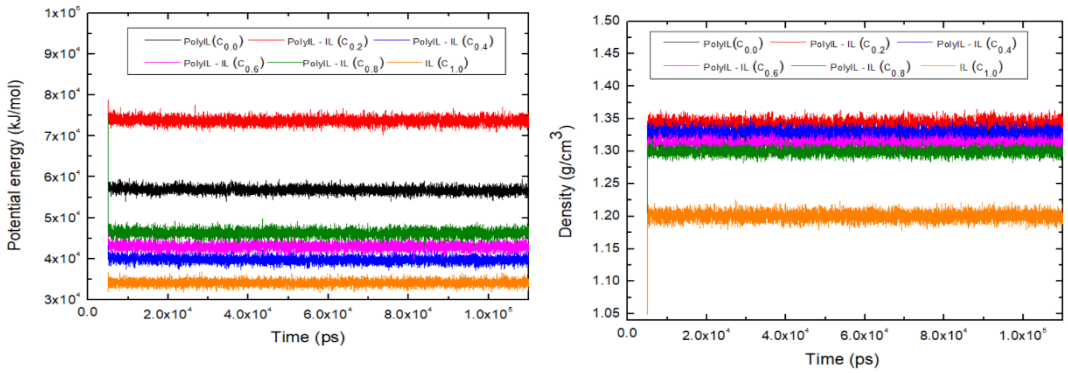

Figure 4.4.1 Time evolution of potential energy (left) and density (right).

4.4.1.2 Radius of gyration (R_g): Molecular size

Results for chain dimension are presented in Table 3.2 and Figure 4.4.2 The R_g and R_{ee} for chains in the PolyIL-IL blend systems decreased slightly from the pure PolyIL. But the value of R_g and R_{ee} for blend systems are a significant decrease. For previous experiment from Matsumuto et al. (Matsumoto, 2019), they studied about the rheological properties of PIL in IL solutions are strongly influenced by the electrostatic screening between IL and PIL chains. These their results indicate that polymerized ionic liquid chains shrink as the ionic liquid concentration increases at lower concentrations due to the charge screening effect by the same mechanism as that for ordinary polyelectrolytes in salt solutions but start to expand at higher ionic liquid concentrations due to the charge underscreening effect. In our study, chains in the PolyIL-IL blends and in the pure PolyIL gave similar R_g and R_{ee} values (see Table 3.2 : Chapter III), and the behavior mentioned above possibly also occurred in our simulated systems.

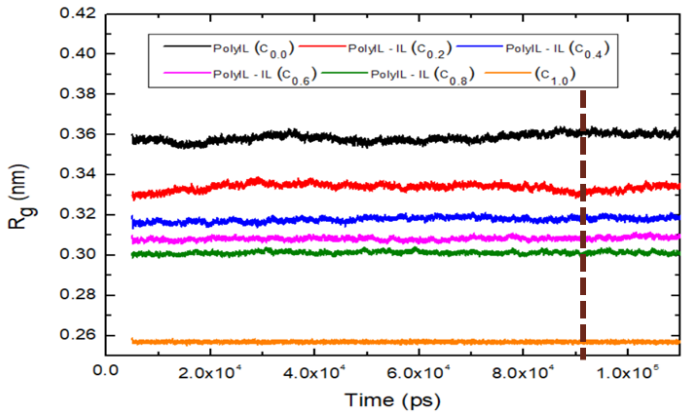

Figure 4.4.2 Time evolution of the radius of gyration (R_g) for IL, PolyIL and PolyIL-IL blends from the 110 ns equilibration runs. The dashed lines indicate the equilibration time of the R_g.

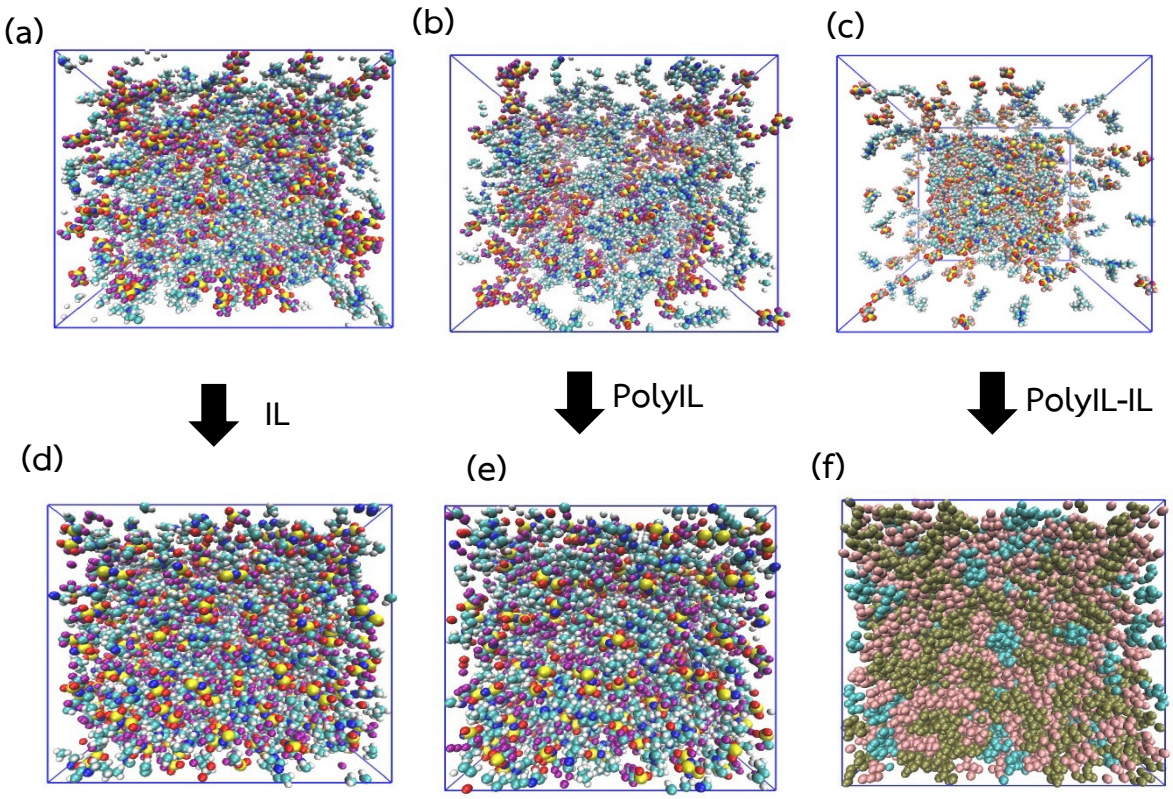

Figure 4.4.3 The initial [non-equilibrium] : (a), (b) and (c) and final structures [equilibrium] : (d), (e) and (f) at 600 K.

4.4.2 Polymer dynamics: PolyIL–IL Blends

4.4.2.1 The mean squared displacement (MSD) and Diffusion coefficient (D)

The dynamics of polymer chains were studied both in terms of translational and orientational mobility. For the definition of MSD at the time of reaching equilibrium at infinity because if the system moves in a straight line, the system enters a diffusive regime, meaning it moves in a straight line with no change in slope. Therefore, if the running time increases but the system's trajectory remains constant, we conclude that time is used in simulation is infinite time of system to reach equilibrium. For the definition of time-dependent diffusion coefficient (D), derived from the mean squared displacement (MSD) using the Einstein relation. Form the results of MSD from figure 4.4.4: (a), (b) and (c), indicated that the translational motion of systems, $BMIM^+$ and

$TFSI^-$ ions increases monotonically with increasing IL concentrations. And $Bmim^+$ has the fastest motion in reaching equilibrium. In additional for figure 4.4.4(d), polycation motions and diffusivities are not easy to obtain for longer polymer chains, we neglect the diffusive calculation of polycations (Zhang, 2020). For the results of diffusion coefficients in Figure 4.4.5(a), (b) and (c), showed that increasing of temperature and concentration of ionic liquids (ILs) effect to improve for diffusion coefficient of all species in PolyIL-IL blends. For figure 4.4.5(d), from the example of diffusion at a temperature of 300 K, it is found that when in the PolyIL system, $TFSI^-$ anions move the fastest. But when ionic liquids are added, the results show that they will be found that cations move the fastest in the blend system but both of $Bmim^+$ and $TFSI^-$ gave similar of diffusion coefficient. Therefore, it can be concluded that the diffusion coefficients increase after adding IL into the PolyIL system and increases temperature.

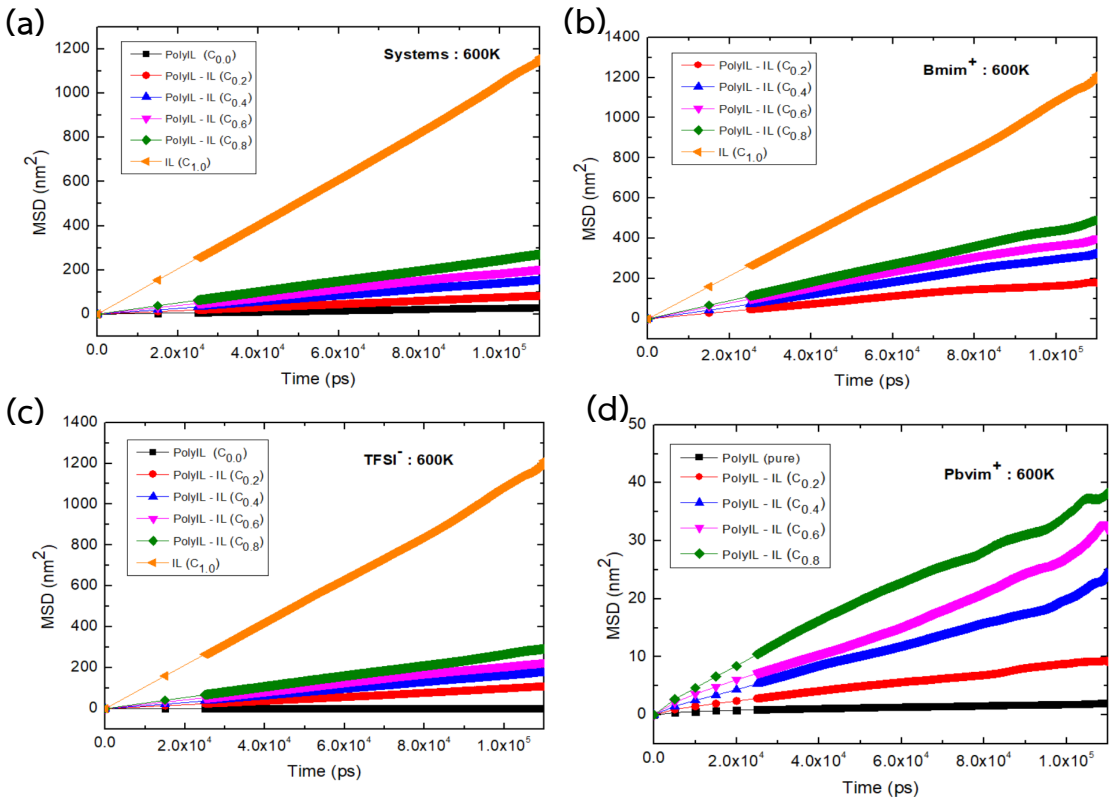

Figure 4.4.4 The mean-square displacement for the center of mass of (a) PolyIL-IL blends, (b) $Bmim^+$ cation, (c) $TFSI^-$ anion and (d) $Pbvim^+$ (polycation).

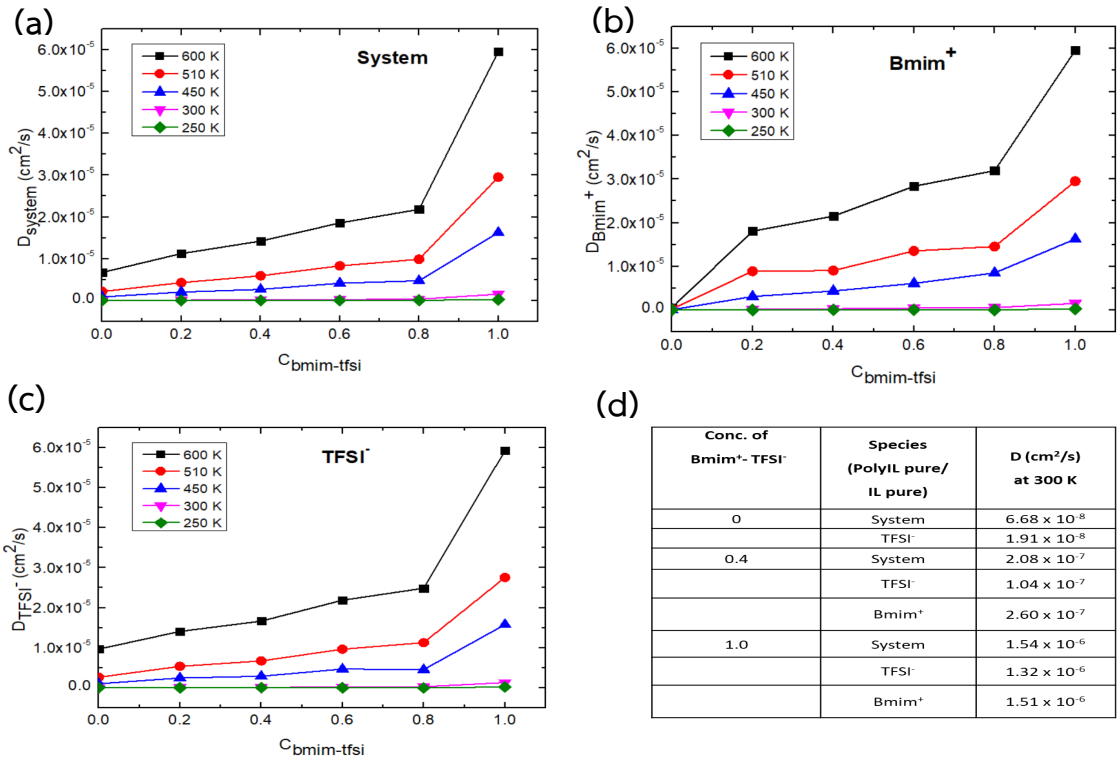

Conc. of $Bmim^+$- $TFSI^-$	Species (PolyIL pure/ IL pure)	D (cm^2/s) at 300 K
0	System	6.68×10^{-8}
	$TFSI^-$	1.91×10^{-8}
0.4	System	2.08×10^{-7}
	$TFSI^-$	1.04×10^{-7}
	$Bmim^+$	2.60×10^{-7}
1.0	System	1.54×10^{-6}
	$TFSI^-$	1.32×10^{-6}
	$Bmim^+$	1.51×10^{-6}

Figure 4.4.5 The Diffusion coefficient of (a) PolyIL-IL blends, (b) $Bmim^+$ cation, (c) $TFSI^-$ anion and (d) Comparisons between PolyIL, PolyIL-IL blends and IL, respectively.

4.4.2.2 Ion Diffusivities for PolyIL–IL Blends

From the results displayed in Figure 4.4.6(a) and 4.4.6(b), we monitor that at all the temperatures examined the diffusion coefficients of both $Bmim^+$ and $TFSI^-$ ions increase monotonically with expanding IL concentrations. Each effect verifies the assumption underlying our research and illustrates that blending polyILs with pure ILs can actually result in an improvement in the ion mobilities relative for ILs. Interestingly, we also note that the enlarge of diffusivities upon addition of pure ILs to polyILs is less than for $TFSI^-$ compared to those seen for $Bmim^+$ ions. Such trends can be understood at a qualitative level by considering that with expanding fraction of ILs, there is a consisting escalate in the number of cations, accrue mobile $BMIM^+$ cations. The coordination of $TFSI^-$ ions to such counterions is expected to lead to a significant

fasting of the dynamics of anions. And In Figure 4.4.6(c) and 4.4.6(d), we display the above diffusivity results in the plane of T/T_g (T_g corresponding to the glass transition at the considered loading of IL). The $TFSI^-$ ion mobilities are seen to display a "decoupling" in this representation.

Explicitly, we observe that the mobilities of polyIL-IL at IL concentrations: 0.2-0.6 and pure ILs are higher (at a specified T/T_g) than the polyIL-IL of IL concentrations: 0.8 at low temperatures because there is a large competition between $Bmim^+$ cations and $TFSI^-$ anions. This can be seen from the Transference Numbers for PolyIL–IL Blends data (Figure 4.4.19 at PolyIL-IL $C_{0.8}$). Both cations and anions have higher transfer values. Therefore, the mobilities of the blend system at 0.8 of IL concentrations is the slowest mobility at low temperature (specified T/T_g) and are sensitive to the loading at high temperatures. The overhead results demonstrate that once the coordination of polycations is soaked, the anions diffuse independently without being affected by the polymer chains and exhibit a decoupling phenomenon. A surprising investigation is that very similar decoupling properties also manifest in the cation diffusivities.

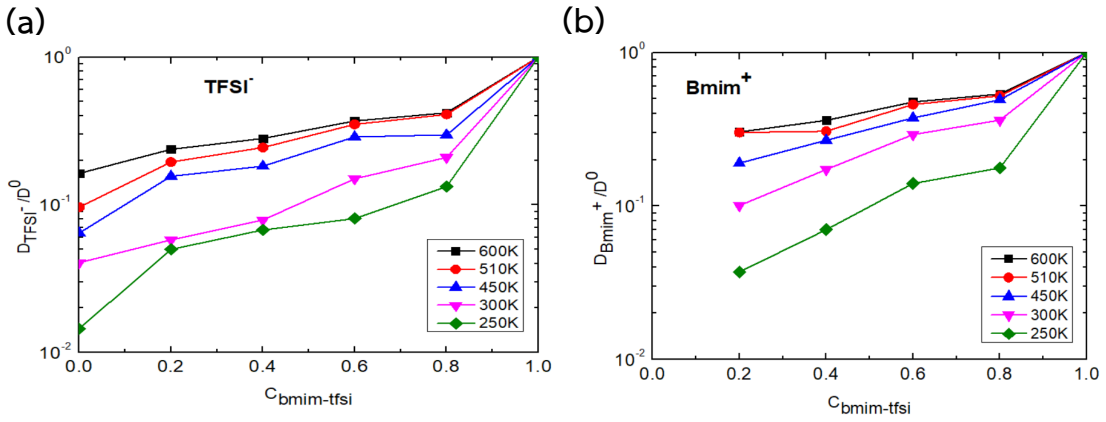

Figure 4.6 The Diffusion coefficient of (a) $TFSI^-$, (b) $Bmim^+$ ions in polyIL–IL blends as a function of IL concentrations at different temperatures. In the figure, D_0 is the respective value obtained for pure ILs. (c) $TFSI^-$ and (d) $Bmim^+$ ions in polyIL–IL blends as a function of T/T_g at different IL concentrations.

(c)

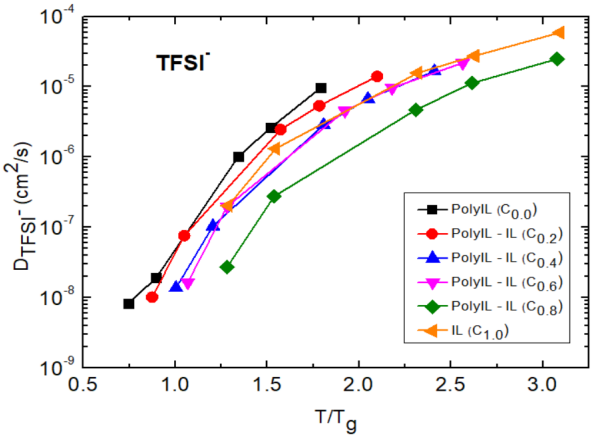

(d)

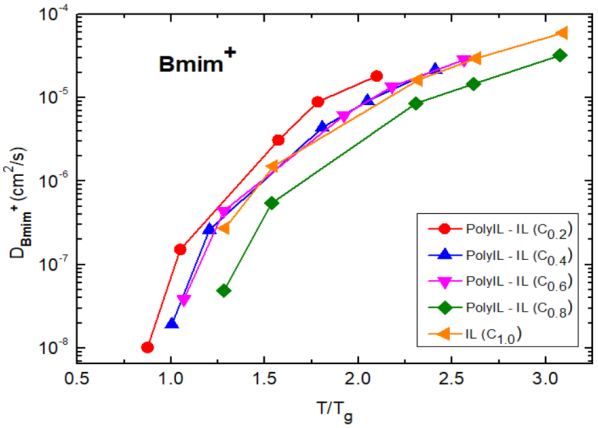

Figure 4.6 The Diffusion coefficient of (a) $TFSI^-$, (b) $Bmim^+$ ions in polyIL–IL blends as a function of IL concentrations at different temperatures. In the figure, D_0 is the respective value obtained for pure ILs. (c) $TFSI^-$ and (d) $Bmim^+$ ions in polyIL–IL blends as a function of T/T_g at different IL concentrations (continued).

4.4.2.3 The orientational autocorrelation functions (ACF) and KWW relaxation times for PolyIL–IL Blends at 600 K

From ACF data as depicted in Figure 4.4.7(a), we observe that the autocorrelation functions of the polymer chains in the blends systems decayed more quickly than that of the pure polyIL system. And then (Figure 4.4.7(b)). we calculated the timescale of backbone auto-correlation function of relaxation times of polymer chains by fitting the Kohlrausch Williams-Watts (KWW) stretched-exponential function (τ_{KWW}) of the polymer as a measure of the polymer segmental dynamics. τ_{KWW}

decreases monotonically with increase in IL concentrations, indicating that the addition of ILs (Bmim-TFSI) indeed facilitates faster segmental dynamics of the polymer chains.

The above results indicate that inspection by advising that the addition of ILs reduce the extent of coordination between the anions ($TFSI^-$) and the polycations ($Pbvim^+$) while expanding the coordination of the anions with the cations ($Bmim^+$). And the relaxation times of polymer chains is consistent with Matsumoto et al. 's research (Matsumoto, 2019). Specifically, they identified three regions, but from MD simulation results are consistent with second region that at an intermediate of c_s (concentration of the ionic liquid Bmim-TFSI), η_{sp} and λ decreased with increasing c_s. These results indicate that polymerized ionic liquid chains shrink as the ionic liquid concentration increases at lower concentrations due to the charge screening effect by the same mechanism as that for ordinary polyelectrolytes in salt solutions. And the phenomena refer to over probably also happened in our simulation models.

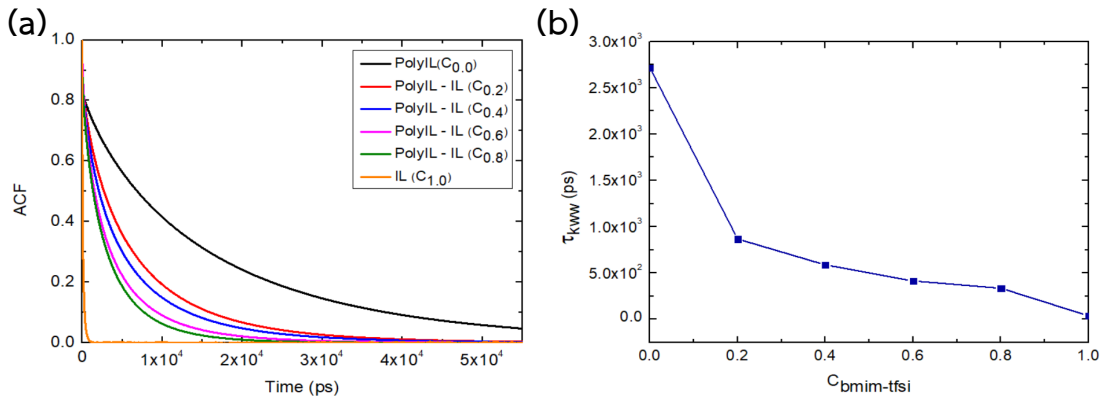

Figure 4.4.7 (a) The Orientational autocorrelation functions and (b) KWW fitting of PolyIL-IL blends in various IL concentrations. Corresponding KWW relaxation times (τ_{KWW}) for each system.

4.4.2.4 Short time dynamics

For Figure 4.4.8, we observe that for as expected, the largest movement is seen for $Bmim^+$ while $TFSI^-$ and the $Pbvim^+$ exhibit a much smaller magnitude of displacement. These results are indicated that $Pbvim^+$, $Bmim^+$ and $TFSI^-$. All three species had improved displacement with the addition of ionic liquids due to when the system are no ionic concentrations, it will be found that the polymer moves very

slowly. This causes the polymer to aggregate together rather than diffusion of their motion. If the ionic concentrations are gradually increased, this will result of each system in the polymer having a better distribution of movement.

And Figure 4.4.9 and Table 4.4.1. For quantitative, the absolute displacement indicate that rigidity of the coordinating structures can be ordered as: $Pbvim^+ < TFSI^- < Bmim^+$. This all data of the absolute displacement for PolyIL–IL Blends at 600 K suggest that $TFSI^-$ interact strongly with the $Pbvim^+$ and move cooperatively on a relatively smaller scale while $Bmim^+$ have much larger amplitudes of the displacement. And the fluctuation indicating that $Bmim^+$ are quite weaker interact with $TFSI^-$ and other species. Therefore, this information will confirm the information mentioned above that indicating that the addition of ILs (Bmim-TFSI) indeed accommodates faster segmental dynamics of the polymer chains.

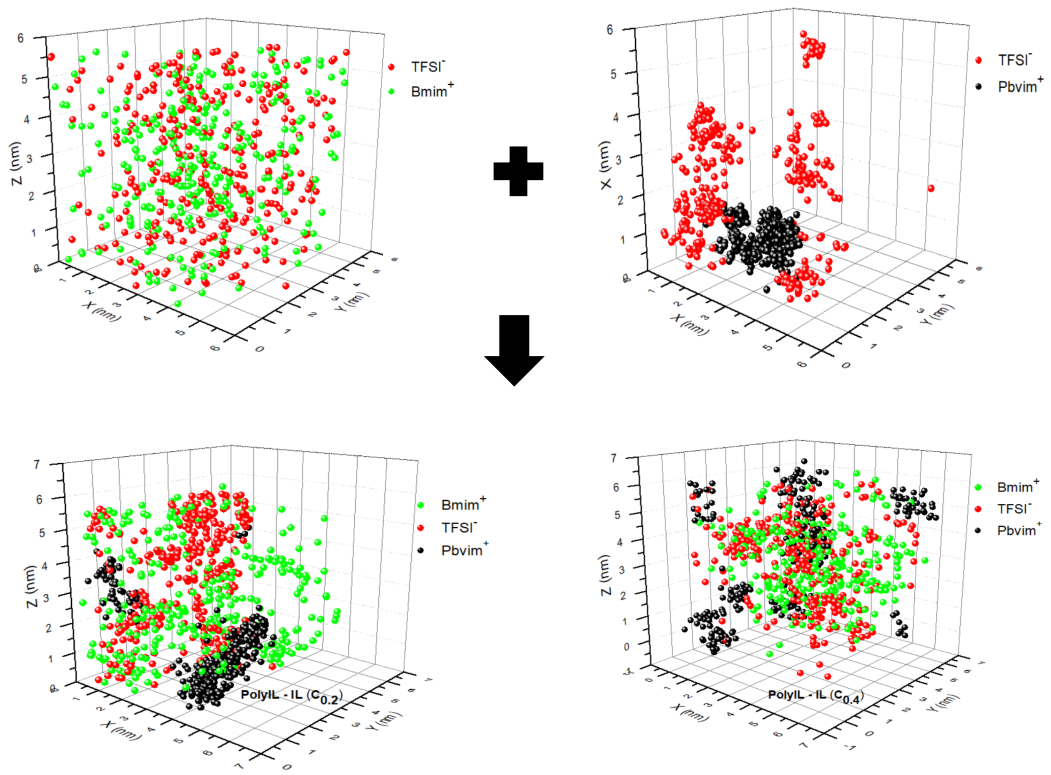

Figure 4.4.8 The Trajectories of $Bmim^+$, $TFSI^-$ and $Pbvim^+$ recorded every 500 ps.

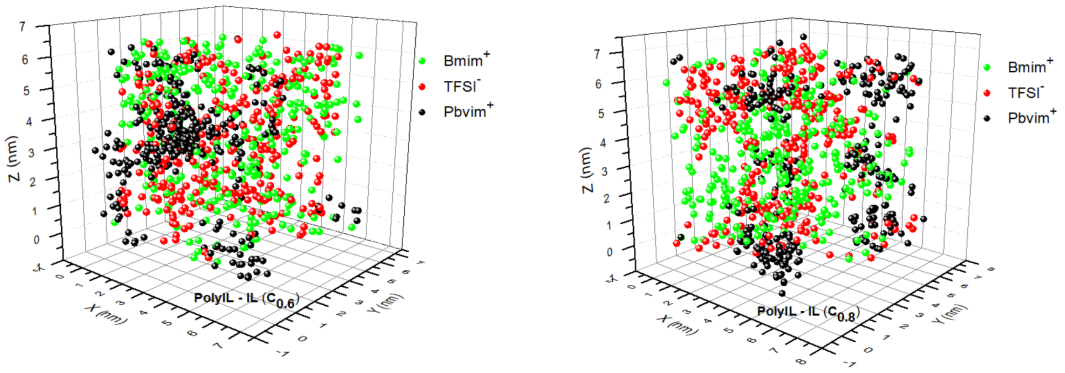

Figure 4.4.8 The Trajectories of $Bmim^+$, $TFSI^-$ and $Pbvim^+$ recorded every 500 ps (continued).

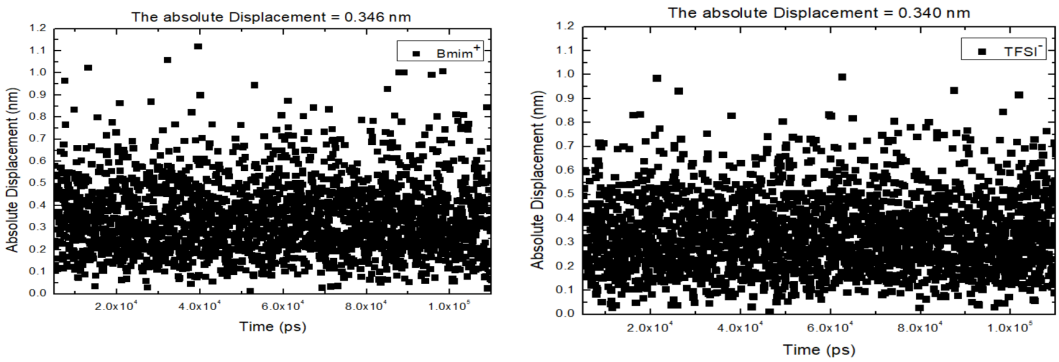

Figure 4.4.9 The absolute displacement of ILs system (a) $Bmim^+$ and (b) TFSI- every 500 ps interval.

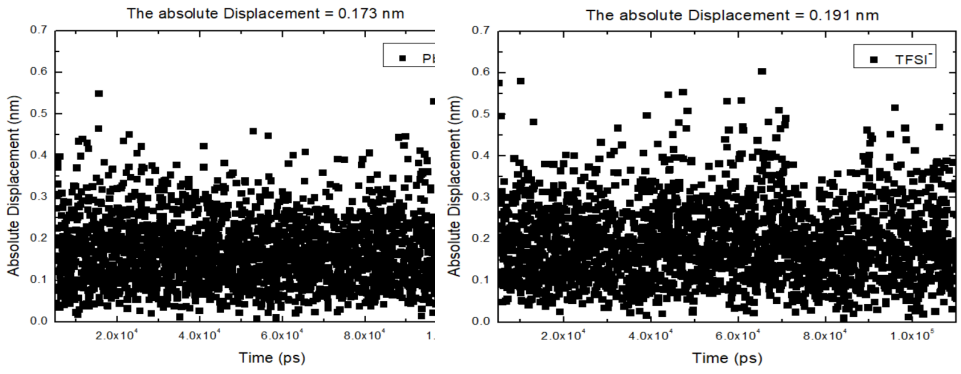

Figure 4.4.10 The absolute displacement of PolyILs system (a) $Pbvim^+$ and (b) $TFSI^-$ every 500 ps interval.

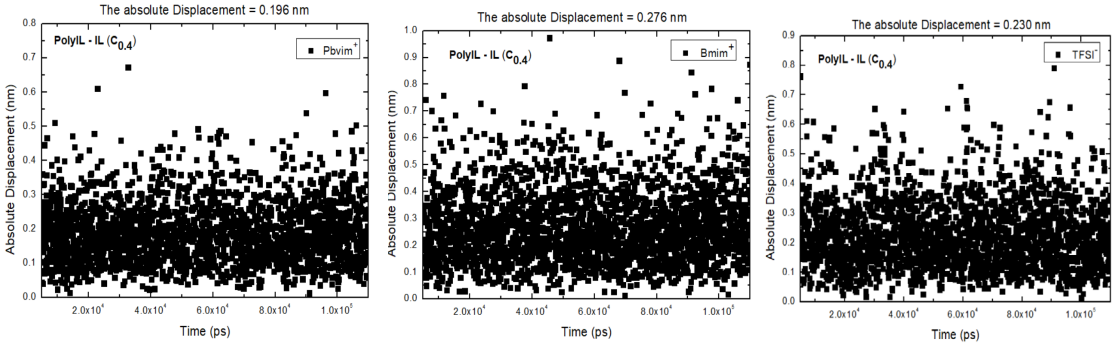

Figure 4.4.11 The absolute displacement of PolyIL-IL system (a) $Pbvim^+$ and (b) $Bmim^+$ and (c) $TFSI^-$ every 500 ps interval; Give an example (at ILs conc = 0.4) of a blend systems from all systems.

Table 4.4.1 The absolute displacement (in 500 ps increments) of ILs, PolyILs and PolyIL-IL blends.

Conc for IL	Species	The absolute displacement (nm)	Conc for IL	Species	The absolute displacement (nm)
IL pure	$Bmim^+$	0.346	0.6	$Pbvim^+$	0.205
	$TFSI^-$	0.340		$TFSI^-$	0.234
0	$Pbvim^+$	0.173		$Bmim^+$	0.286
	$TFSI^-$	0.191	0.8	$Pbvim^+$	0.210
	$Bmim^+$	-		$TFSI^-$	0.246
0.2	$Pbvim^+$	0.185		$Bmim^+$	0.296
	$TFSI^-$	0.216	1.0	$Pbvim^+$	0.217
	$Bmim^+$	0.259		$TFSI^-$	0.270
0.4	$Pbvim^+$	0.196		$Bmim^+$	0.305
	$TFSI^-$	0.230			
	$Bmim^+$	0.276			

4.4.3 Radial Distribution Functions (RDF) and Coordination numbers (CN)

For RDFs, the illustrative atoms chosen for anion, cation, and polycation were identical to those adopted for the analysis of the mean squared displacement (MSD) and Diffusion coefficient (D). Further, the cutoffs for evaluating the anion–cation/polycation coordination were determined by the position r where g(r) = 1.0 after the first peak (Zhang, 2020). From the results in Figure 4.4.12(a), we see that the value of peak for the association of $Pbvim^+$ - $TFSI^-$ is higher than that of $Bmim^+$ - $TFSI^-$, indicating a stronger binding of $TFSI^-$ with the $Pbvim^+$ monomers attached to the

polyIL chains at the same temperature, indicating that IL concentrations are dominated. With results confirming this behavior by the absolute displacement in Figure 4.4.9, 4.4.10 and 4.4.11. For Figure 4.4.12(b), at the same temperature, it is found that the CN of ILs increases and decreases in the polyILs systems with increasing ILs concentration.

In summary for RDFs and CNs can be found that at the same temperature, It will indicate that for polymers and anions, the interaction becomes more gradually stronger as the ionic concentrations increases because the ILs will help the anions move along the polymer faster. And from the behavior mentioned above, the binding of IL will gradually decrease because the cations will interact with the anions to help the anions move faster.

After that, we were studying RDF at different temperatures. For Figure 4.4.13(a), 4.4.13(b) and 4.4.13(c), this indicates that there is no difference in both polymer and ionic properties. Therefore, we can be concluded that the ILs concentration is more prominent than the effect of temperature.

For Figure 4.4.14(a), we observe that CNs data indicate a decrease in the $Pbvim^+$ system enclosing $TFSI^-$ because $TFSI^-$ are switched to bind with $Bmim^+$. From Figure 4.4.14(b), it will be found that when the temperature is increased, the value of CN changes very little. We can be concluded that the IL concentrations is more prominent than the effect of temperature.

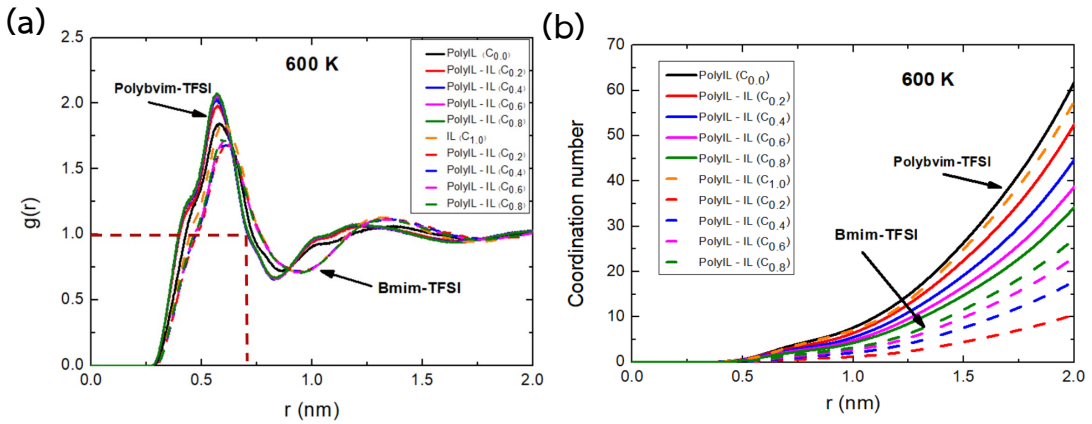

Figure 4.4.12 Radial distribution function between (a) the centers of mass for $Pbvim^+$, $TFSI^-$and $Bmim^+$ and (b) Coordination numbers (CN) at 600 K.

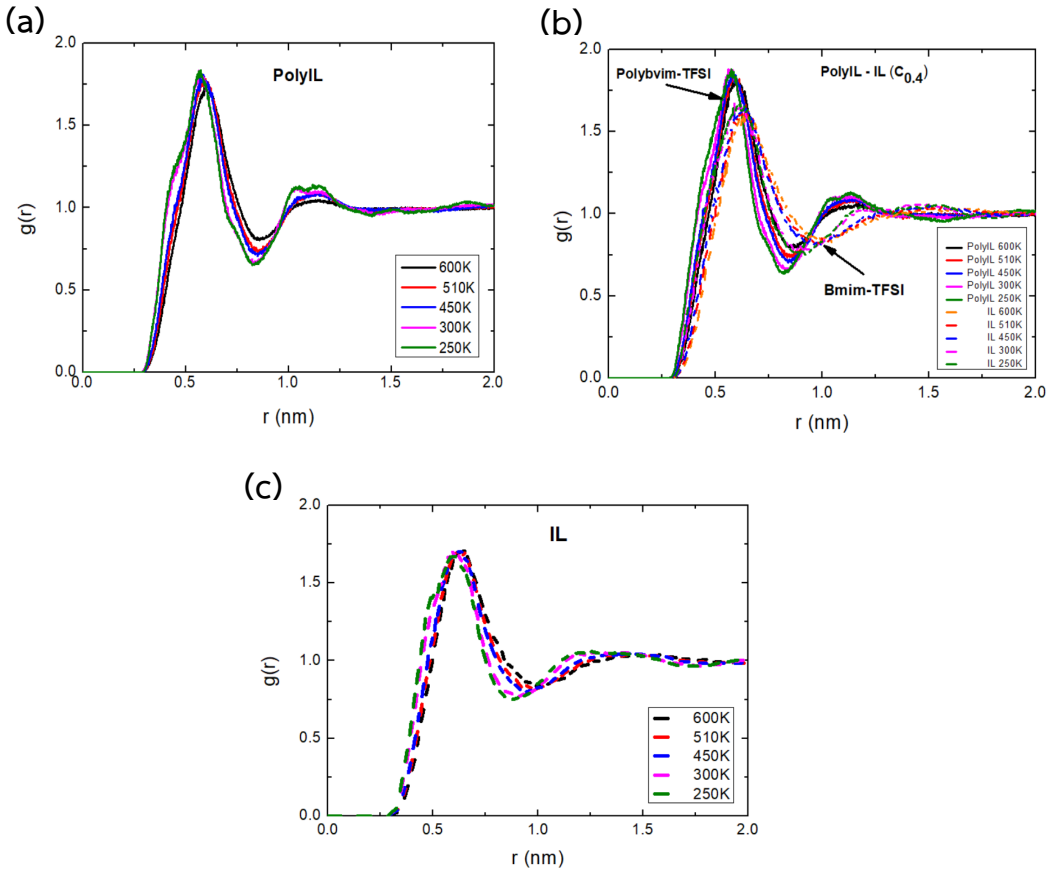

Figure 4.4.13 Radial distribution function between (a) the centers of mass for PolyILs, (b) PolyIL-IL blends and (c) ILs at different temperatures.

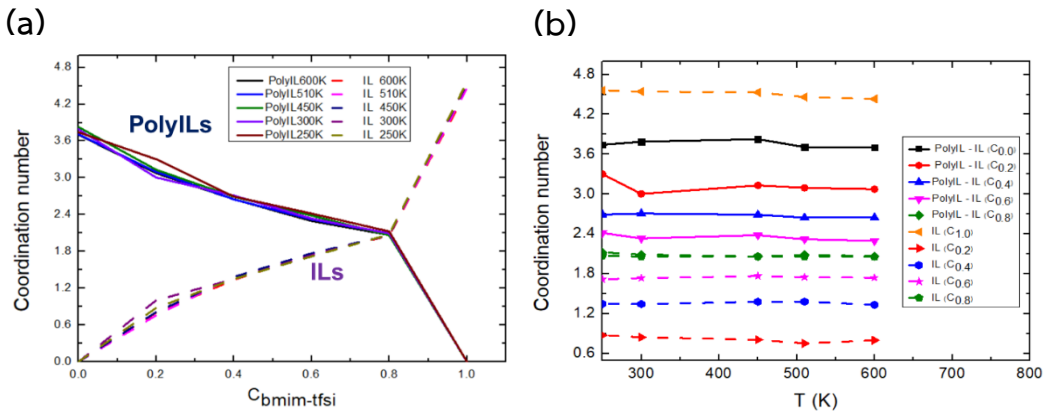

Figure 4.4.14 Coordination numbers (CN), (a) for PolyILs, ILs at different IL concentrations and (b) for PolyILs, ILs at different temperatures.

4.4.4 Ion Transport Mechanisms

4.4.4.1 Anion Association Statistics

To understand the influence of IL concentrations (Bmim-TFSI) on the $TFSI^-$ coordination characteristics, we calculated the probability, P_n, that a given $TFSI^-$ is associated with n cations/polycations and the probability P_N that an anion is associated with N number of chains at different loadings of the ILs electrolyte at 600 K. Form Santosh et al (Mogurampelly, 2018). In the absence of polymer chains (i.e., pure ILs), the anions are expected to be in only one of two states: (a) stay free from any kind of association; (b) associate with non-polymerized cations. Whence, for pure ILs, P_N and P_n are expected to be zero for N, n > 0.

It is observed from Figure 4.4.15(a), that P(n) exhibits a maximum at n = 4 in the absence of pure ILs. However, as the IL concentrations increases, the location of the peak is seen to gradually shift to n = 3, while the association with four cations constitutes the second major coordination group. For blend systems display peaks of P(n) at n = 3 and n = 2, suggesting that such anions swap out either one or two cations and engage with non-polymerized cations as a third and/or fourth partner for their coordination. Moreover, when increasing IL concentrations show that the number of free ions IL concentrations larger than low IL concentrations.

Next, we turn to the influence of IL concentrations on the coordination of anion with distinct polymer chains in Figure 4.4.15(b), we quantify such features through the consideration of the probability P_N that an anion is coordinated with N distinct polymer chains. This data show that peak of P_N at N = 2 is observed in the absence of IL concentrations. Further, with an increase in IL concentrations, the peak is seen to transition from N = 2 to N = 1. PolyIL-IL blends are seen to preferentially associate with a single polymer chain. Together, the results of the coordination statistics presented in Figure 4.15 and Figure 4.4.16 suggest that the co-coordinated anions dissociate from the second polymer chain and instead preferentially engage in coordination with the cations of a single polymer chain.

In summary for anion association statistics. From the both graphs of Figure 4.4.15 indicate that, when increasing the concentration of ionic liquids, P_N and P_n are

seen to peak at N = 2 and n = 4, indicative of the anion association with four monomers of two different polymer chains in pure polyIL electrolyte. And P_N and P_n exhibit a maximum for N = 1 and n = 3 or 2, suggesting that a given anion prefers to be associated with three polymerized cations of the single polymer chain in PolyIL-IL Blends. The decreasing of number of cations and polymer chains associated with anion because there is a switching of the coordinated interaction of anions between the polymer chains and cations.

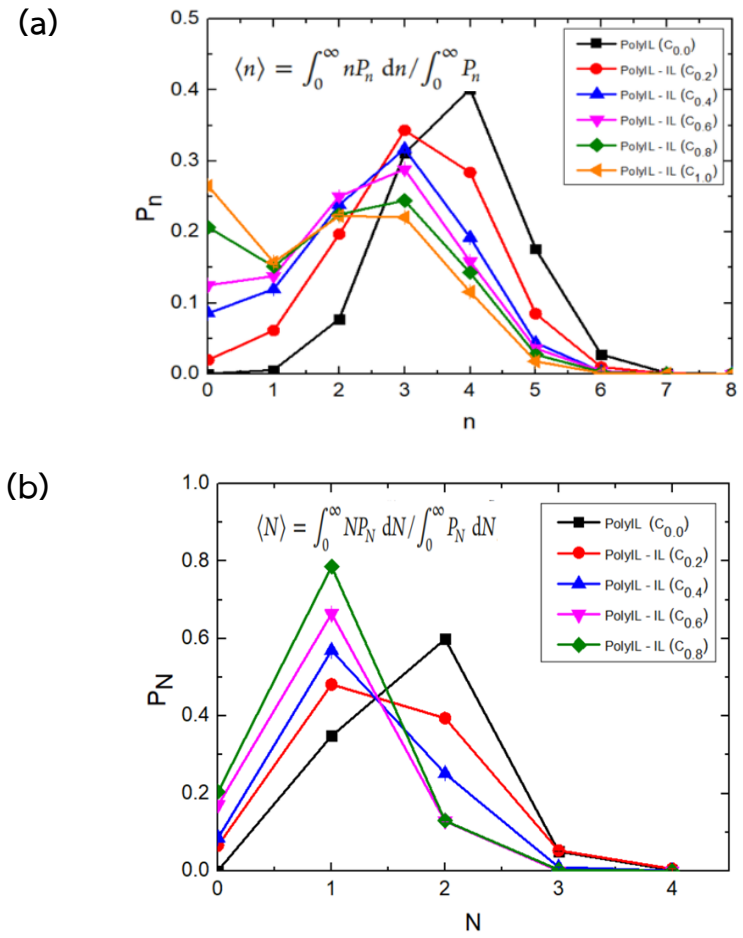

Figure 4.4.15 Probability that a given $TFSI^-$ is associated with (a) n cations and (b) N polymer chains. The error bars are smaller than the size of the symbol where invisible.

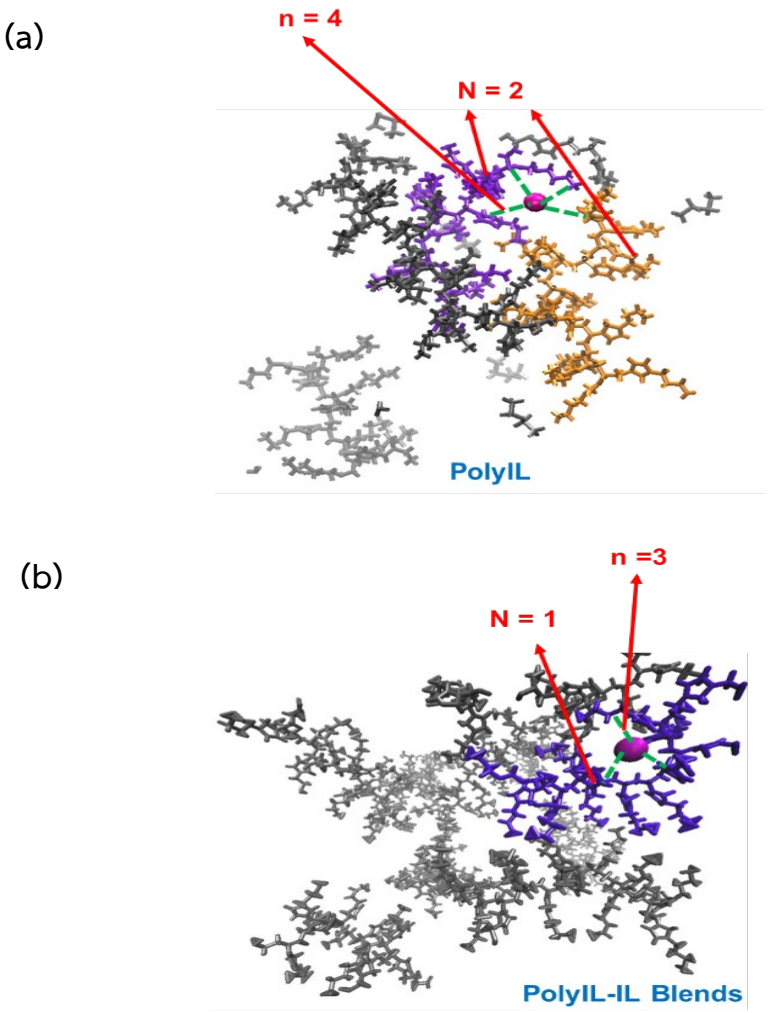

Figure 4.4.16 A snapshot of anion (magenta) association to polymerized cations and polymer chains in (a) PolyIL and (b) PolyIL-IL blends. The represent an ion-association determined from a distance cutoff of 6.5 Å. Only the polymer chains within 20 Å spherical radius from the centered anion are shown without any other ions for clarity.

4.4.5 Glass Transition Temperatures (T_g) for PolyIL–IL Blends:

The blend systems were then cooled from 600 K stepwise to 160 K by decrements of 10 K. Using cooling rate = 1 x 10^{10} K/s and the system density was calculated from the last 1ns from 2ns of NPT simulation (Mogurampelly, 2017). The increase of $V_{specific}$ with increasing temperature was less pronounced below T_g yielding a kink separating rubbery and the glassy states (Khongvit, 2020).

T_g values for all simulated systems are presented in Figure 4.4.17. The T_g for all blend systems were lower than for the pure polyILs. For all the $V_{specific}$ curves have only one transition between the high- and low-temperature regimes. One transition is usually interpreted as evidence of miscibility, while two transitions imply immiscibility of polymers (Kikkawa, 2009; Thomas, 2014; Saha, 2016). The fact that only one kink is observed in the $V_{specific}$ curves argues for miscibility of PolyILs, ILs and PolyIL-IL blend systems. In Figure 4.4.18(a), T_g from experiment show that the all blend systems have two glass transition temperature (T_g) follows as T_g low and T_g high. Because T_g from blend systems have broad range, when increasing temperature make them transform glassy state to the liquid state indicated that enriched local concentration of polyIL are dominantly, so this effect is called T_g, high and when decreasing temperature make them behavior like float state indicated that enriched local concentration of ILs are dominantly, so this effect is called T_g, low.

And what's interesting is that when calculating the T_g value for pure ILs and pure polyILs in Figure 4.4.17, it was found that both linear lines are very good. But when observing the blend systems, we were finding that both lines of high and low temperature deviate from the linear lines. We hypothesize this phenomenon that the simulated results may behave like the experimental results, so the broad range is the cause of the two lines leading to T_g line of both temperatures deviating from the linear line.

The generally, polymer blends can be divided into three categories: miscible, semimiscible (or partially miscible), and immiscible blends (Thomas, 2014). A blend of miscible polymers exhibits a single T_g as well as a single homogeneous phase. Two distinct T_g values arising from two phase-segregated components are often interpreted as an indicator of immiscibility (Kikkawa, 2009; Thomas, 2014). An alternative view has been proposed by Lodge and McLeish (Lodge, 2000). According to their self-concentration model, chain connectivity of polymers leads to an increased local concentration of monomers in blends compared to an average bulk concentration. For this reason, one should normally expect two glass transitions in any single-phase

polymer blend. Thus, it was suggested that the presence of two distinct T_g values cannot be used as a reliable criterion of immiscibility and semimiscibility (Lodge, 2006).

Together, the results discussed above indicate that we cannot say all blend systems have separated because in simulation results show that all snapshots were created using VMD open-source software, the polyIL-IL blend systems are homogeneous. But in the experimental results of T_g, the high T_g and the low T_g blend components exhibit, respectively, stronger and weaker variations with the blend composition. As already mentioned, we believe that the estimates of $\{T_g\}$ obtained from relaxation time and specific heat measurements may be different. Jacek et al, their theory predicts that spontaneous concentration fluctuations may lead to the appearance of two mesoscopic regions of enriched local concentration in macroscopically homogeneous, but locally inhomogeneous, one-phase binary polymer blends. These mesoscopic concentration fluctuations, a universal property of blends of semiflexible polymers not shared by mixtures of non-associating small molecule liquids. Moreover, the relatively large concentration fluctuations naturally explain the existence of two relaxation time and two T_g in miscible blends with sufficient dynamical asymmetry between the blend components (Jacek Dudowicz, 2014).

In Figure 4.4.18(b). When the experimental results are compared with the simulation results. It was found that the simulation results for T_g in good agreement with experimental values.

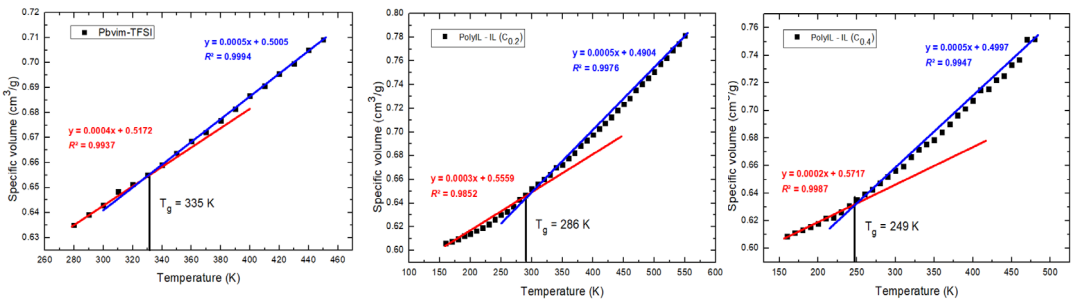

Figure 4.4.17 Plots of specific volume versus temperature to determine Tg values for various IL concentrations of blend systems.

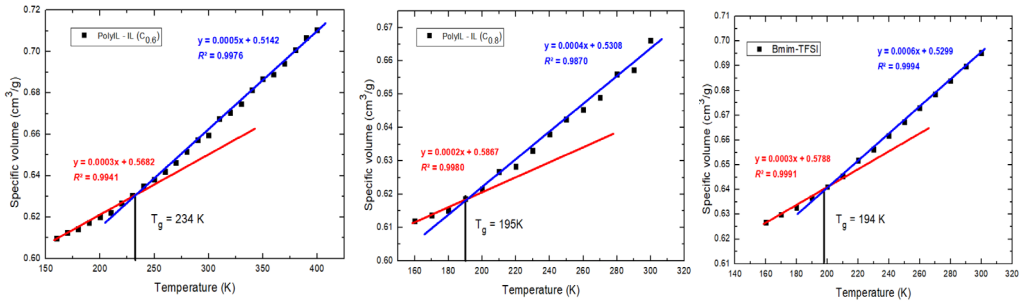

Figure 4.4.17 Plots of specific volume versus temperature to determine Tg values for various IL concentrations of blend systems (continued).

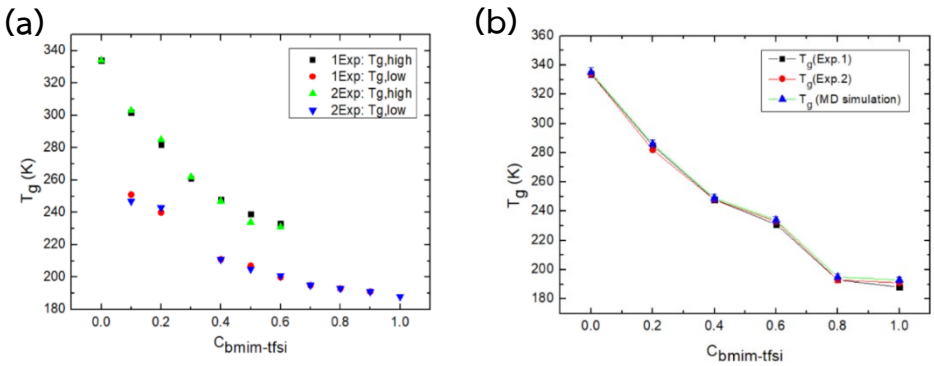

Figure 4.18 (a) T_g from experiment and (b) Comparison (Exp.& Sim.) of Glass Transition Temperatures (T_g).

4.4.6 Transference Numbers for PolyIL–IL Blends

Amount of relevancy in defining the accomplishment of polymer electrolytes is the transference number. The transference number amounts the current transported by the identity of attention (in our case, the anion) relative to the overall current. Each a number is of regard as its relevancy in quantifying the predisposition for concentration polarization features resulting from the evacuation and hoarding of the contrast charged ions at the electrodes (Mogurampelly, 2018). While several definitions of transference number exist (Balsara, 2015), in the present context, we use the definition that only relies on ion mobilities and the number of mobile species.

From Figure 4.4.19(a) and 4.4.19(b), we can observe that the transfer numbers of $TFSI^-$ anion have irregular fluctuation as the temperature increases. Addition of mobile ions, such as in our case through the cations of pure IL, is prospective to increase the conductivity but concurrently lower the transference numbers of $TFSI^-$ anion. Each

datum is surprising, as one would have prospective that the transference numbers would display a monotonic inflate with ILs adding to the value of unity for pure ILs. Again, our results illustrate a recantation arising from effect with enlarged ILs loading and temperature, viz., the increasing of the anion mobilities relative to the cations.

For polyIL, we will be found that polycations move very slowly. Therefore, anions are highly transferable. Therefore, it is to move like a free ion in the simulation. Then when they come to a blends system is to add ILs. Therefore, a competition occurred between polycations or cations with anions. And then there is a change in the coordination numbers of anions, which is to switch between polycations and anion or cation and anion. For pure IL, there will be a very poor amount of anion transfer because anions interact with cations because they have the same number of both. So, we can be concluded that transference numbers of anions have the addition of pure ILs to pure polyILs as the dominant than influence the temperature.

From Figure 4.4.20, all graphs regarding the transfer number of anions. It will be higher than cations because anions are more numbers than cations at PolyIL-ILs (0.0-0.8). And there will be a gradual decrease in transfers until the number of cation and anion ions is equal at PolyIL-ILs (1.0). It is found that cations have a higher transfer amount than anions because cations have more diffusion. And there will be equal transfer at a temperature of 600 K. In their recent study (Zhang, 2020), their found that, even with relatively long-time simulation times extending 400 ns, polycation diffusivities are not easy to obtain for longer polymer chains (Zhang, 2020). Therefore, we find that the simulation time 110 ns run of our simulation systems is sufficient to reach equilibrium with other ion species. Because even if it takes more time to run longer than 110 ns, it will hardly affect the diffusion of the long polymer chain.

For transference Numbers for PolyIL–IL Blends data, it was found that when increasing the ionic concentration, there will be a gradual decrease in the transfer of anions. This is the result of binding with cations to help move them along long polymer chains. Therefore, all information will indicate in evaluating the efficiency of this system that only ion transfer cannot be used in studies alone. The information in Sections 4.4.1-4.4.5 and 4.4.7, as well as simulation trajectory, must be used to more accurately confirm the behavior of the mixed system.

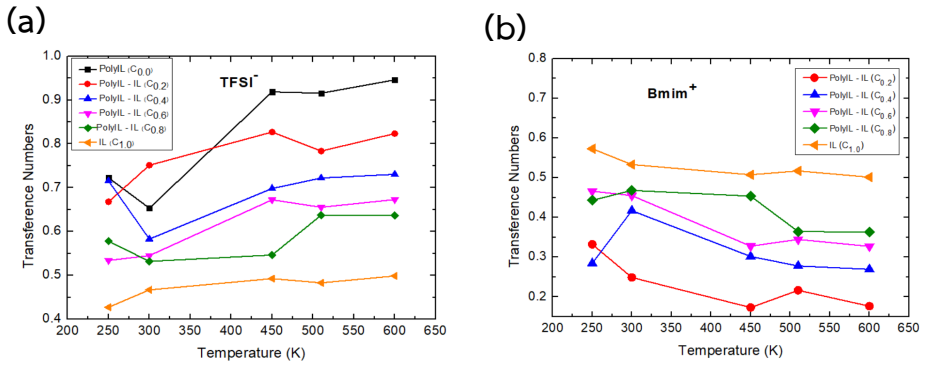

Figure 4.4.19 (a) the anions and (b) cations transference number as a function of the ILs loading at different temperatures.

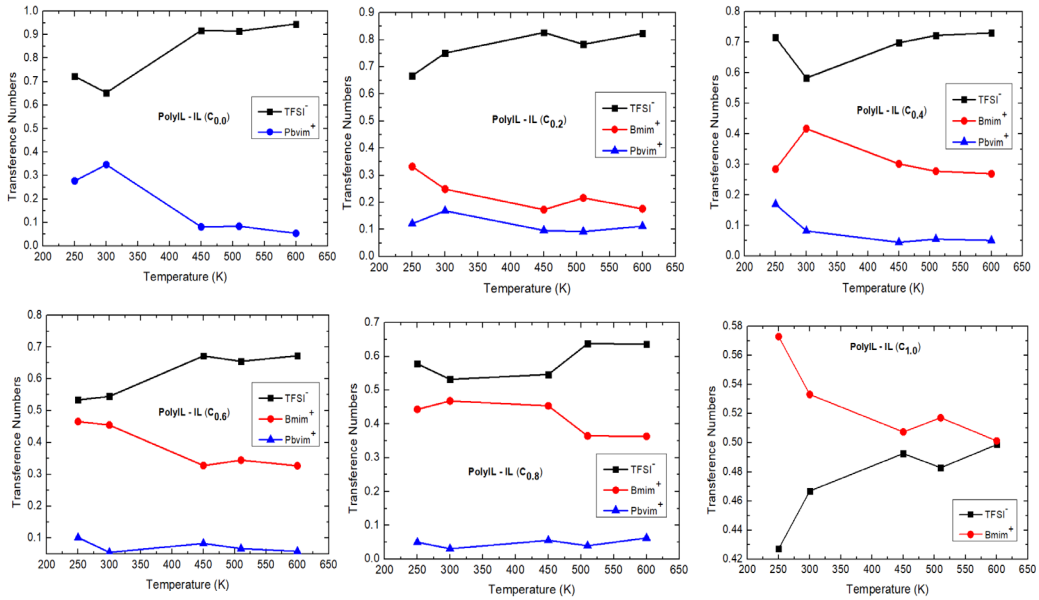

Figure 4.4.20 The comparison of the anions and cations transference number as a function of the ILs loading at different temperatures.

4.4.7 The ideal ionic conductivity in PolyIL-IL Blends

In Figure 4.4.21(a)–(d) and Table 4.4.2, we display the experiment and simulation results for the total ionic conductivity and the NE values as a function of the IL concentrations, respectively.

For Figure 4.4.21(a) and 4.4.21(b), when the experimental results are compared with the simulation results. Although the large numerical errors would make the values of conductivities unreliable, we found that this trend was observed [66]. It was found that the simulation results for the ideal ionic conductivity in good agreement with experimental values in qualitative.

In all results from Figure 4.4.21(a)-(d) and Table 4.4.2, we can confirm that the hypothesis underlying our work and demonstrates that blending pure ILs with polyILs can indeed lead to an enhancement in the conductivity relative to ILs. Therefore, it can be concluded that the ionic conductivity increases after adding IL into the PolyIL system and increases temperature.

Interestingly, in Figure 4.4.22(a)-(c), we show that the NE conductivities exhibit a "decoupling" from T/T_g, the degree of such effects becomes significantly reduced when compared to the ion mobilities (Figure 4.4.6(c)-(d)). Indeed, the conductivity of polyIL-IL blends and pure ILs are still seen to be greater than that of the pure polyILs. And the NE values display a nonmonotonic behavior as a function of pure ILs loading (exhibiting a maximum around 100% ($c_{bmim\text{-}TFSI}$ =1.0) loading of pure ILs). Such trends can be understood to arise as a consequence of the competing effects of the increased number of mobile ions resulting from the addition of pureILs (to polyILs) and the greater mobilities (at a specified T/T_g) of the systems containing a greater fraction of pure ILs.

At this time, there is no clear reason why the simulated conductivity values are too high from the experimental values. Many assumptions have been made in various studies regarding conductivity in simulations such as Neglecting ionic correlations between free ions, intrinsic into the Nernst-Einstein equation, seemingly overestimates the ionic conductivity and on the other hand, ignoring the contribution from bound ions would underestimate the conductivity. But no clear conclusion. Even if the cross-

correlation term is taken into account or the simulation run time is longer, there are still large errors.

Thus, the simulations may be missing some key dynamical aspect. Additional studies using more advanced techniques and force fields may help discover the source of the differences. Nevertheless, the simulation will focus on describing qualitative data for ionic conductivity and Nernst–Einstein conductivities and offer insight at the molecular level.

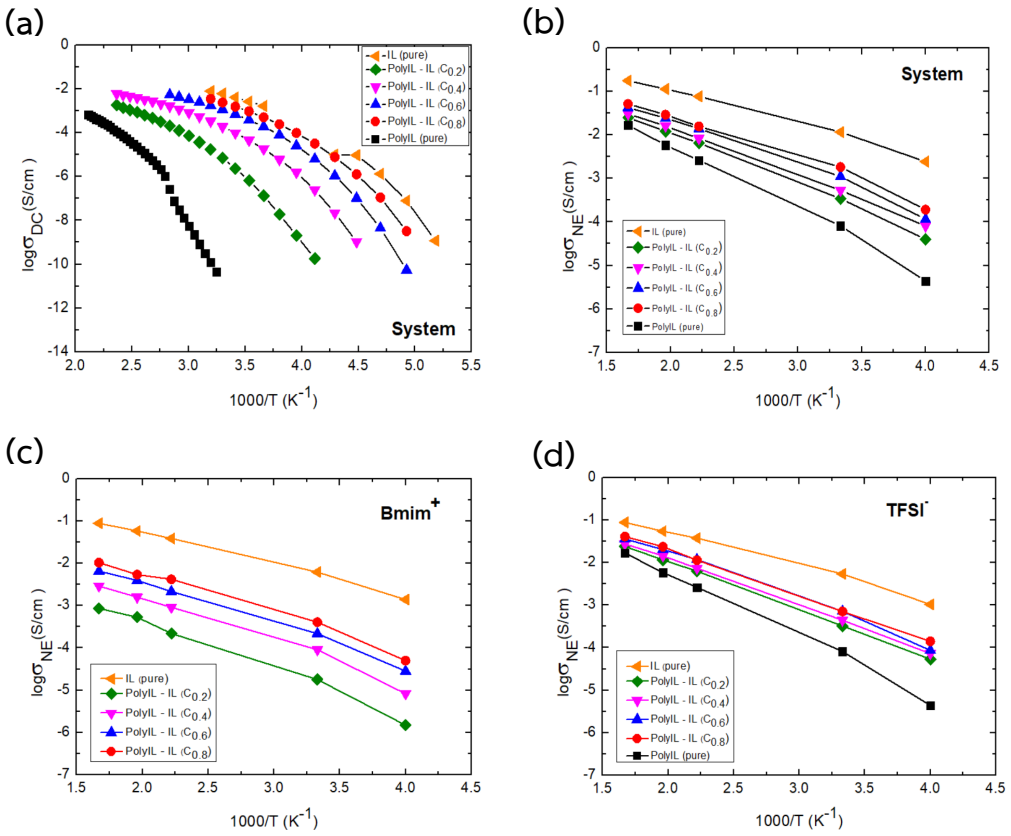

Figure 4.21 The ideal ionic conductivity of PolyIL-ILs blend systems obtained as plotted versus 1000/T (a) Total ionic conductivity from experiment, (b) Total of systems, (c) $Bmim^+$ and (d) $TFSI^-$ for ideal ionic conductivity from MD simulation.

Table 4.4.2 Comparison between the total ionic conductivity from the experiment and the ideal ionic conductivity from MD simulation of PolyIL-ILs blend systems at different temperatures.

Conductivity		MD Simulations (S/m)					Experiments (S/m)
Pbvim-TFSI (pure)	Species	600K	510K	450K	300K	250K	453K
	system	1.685	0.579	0.261	0.00813	0.000437	0.037
	$TFSI^-$	1.685	0.579	0.261	0.00813	0.000437	
Mix0.2 Concentration of Bmim-TFSI	Species	600K	510K	450K	300K	250K	303K
	system	2.487	1.205	0.649	0.0341	0.00398	0.000698
	$TFSI^-$	2.401	1.152	0.627	0.0323	0.00383	
	$Bmim^+$	0.0858	0.053	0.0219	0.00178	0.000149	
Mix0.4 Concentration of Bmim-TFSI	Species	600K	510K	450K	300K	250K	303K
	system	3.028	1.593	0.826	0.0531	0.00806	0.0187
	$TFSI^-$	2.739	1.435	0.735	0.0441	0.00724	
	$Bmim^+$	0.289	0.158	0.0909	0.00902	0.000824	
Mix0.6 Concentration of Bmim-TFSI	Species	600K	510K	450K	300K	250K	303K
	system	4.231	2.424	1.389	0.110	0.0115	0.116
	$TFSI^-$	3.579	2.025	1.175	0.0836	0.00863	
	Bmim	0.652	0.393	0.215	0.0262	0.00282	
Mix0.8 Concentration of Bmim-TFSI	Species	600K	510K	450K	300K	250K	303K
	system	5.12	2.956	1.555	0.434	0.0191	0.237
	TFSI	4.085	2.357	1.136	0.231	0.0141	
	$Bmim^+$	1.035	0.539	0.419	0.203	0.00499	
Bmim-TFSI (pure)	Species	600K	510K	450K	300K	250K	303K
	system	17.542	11.271	7.616	1.158	0.243	0.4878
	$TFSI^-$	8.749	5.442	3.751	0.541	0.104	
	$Bmim^+$	8.793	5.829	3.865	0.618	0.139	

(a)

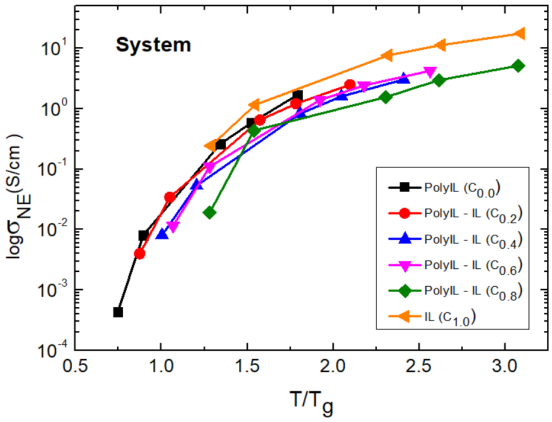

(b)

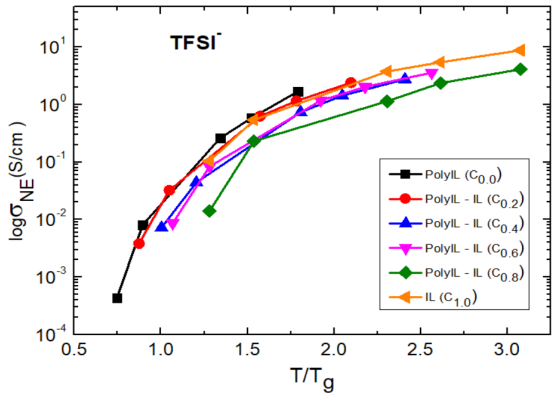

(c)

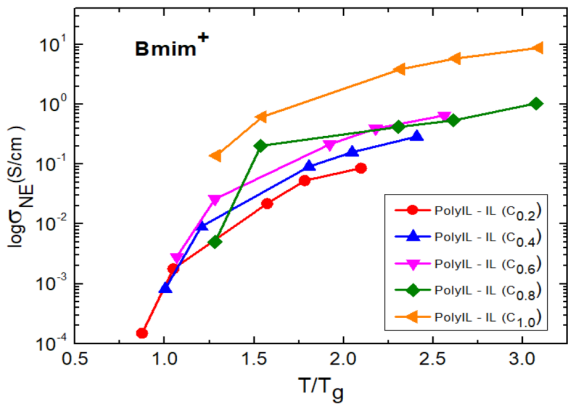

Figure 4.4.22 The Nernst–Einstein predictions a function of the loading of ILs for (a) system, (b) $TFSI^-$ and (c) $Bmim^+$ as a function of T/T_g.

4.4.8 Ion Transport Events in PolyIL-IL Blends at 600 K

To realize the mechanisms underlying union movement in the polyIL electrolytes, we also examined different hopping cases, revealed by the anions which are especially correlated with polymerized cations (Mogurampelly, 2018). To this aim, we degraded the transport cases into three principal categorizations as schematically displayed in Figure 4.4.23: (a) type 1: anion hopping events along polymer backbone by means of the formation and breaking of ion pairs with polymerized cations; (b) type 2: ion hopping events between different polymer chains; and (c) type 3: the to and from transition events occurring between the polymer chains and the rest of the medium; i.e., if an anion is coordinated to polymer chain(s) at time t and uncoordinated to any polymer chain at a different time t′, then it is a type 3 event and in the absence of polymer chains (i.e., pure ILs), the anions are expected to be in only one of two states: (i) stay free from any kind of association; (ii) associate with non-polymerized cations.

From Figure 4.4.24, we observe that intrachain interaction gradually decreased but it is still a dominant mechanism because discussion in Section 4.4.2 in the subtopic is short time dynamics and Section 4.4.3, the interactions between anions and polycations are seen to be stronger than those between anion and non-polymerized cations. After that, competition between polycations and cations arose that compete to form bonds with anions where the main movement is anions interact to polymer chains so it will be the behavior of prominent intrachain hopping.

Later, ionic concentrations were added, this causes the cation to escape from the anion in the free state. The cations then compete for bonding with the polymer chains, this effect causes anions to escape from the polymer chains. And then binds with cations at a certain time. Therefore, this type 3 of behavior is second only to intrachain hopping. And another possible movement behavior is type 2 is the formation of bonds between anions and different polymer chains. From the MD simulation results, it was found that this was the least likely to happen due to the larger number of available non-polymerized cations.

From Inoue et al. (Inoue, 2013), they explained about sub-Rouse mode and proposed that the observation of these local motions is caused by the plasticizing

effect by dissociated large counter-anions. They showed that sub-Rouse mode is often observed for solutions where intrachain interaction is dominant for local motions. Appearance of the sub-Rouse mode for PC_4VITFSI was attributed to the decreasing of interchain interaction due to ionized large counterions which behaves like a solvent.

From the experimental research referenced above. It was found that the movement of PC_4-TFSI, this indicates that there is intrachain interaction that is more prominent than interchain interaction. This is consistent with MD simulation results, indicating that both pure polyIL and polyIL-IL blends, there are prominent intrachain interaction in the movement.

Altogether, the results introduced upon approve us to conclude the mechanism of anion motion in polyIL–IL blend electrolytes. Especially, the all effects indicate a moderate transition in which adding polyILs to pure ILs leads the way a raised tendency of connection of anions with polymerized cations, first of a single chain and then of two chains.

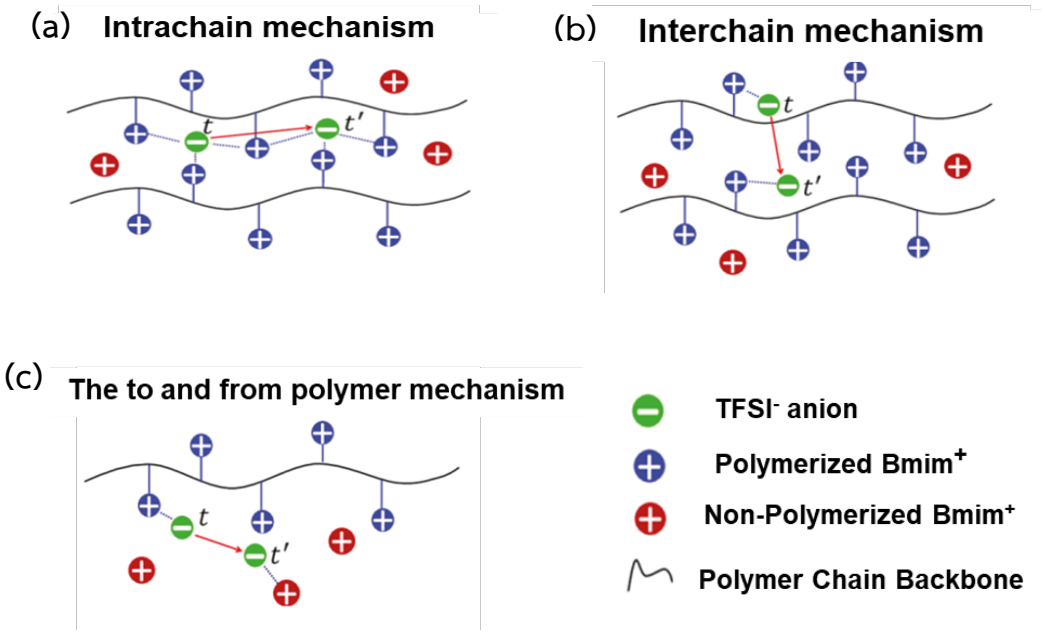

Figure 4.4.23 Definition of ion hopping mechanisms adopted in this work to distinguish different types of ion hopping events in polyIL–IL blend electrolytes from Mogurampelly et al. (Mogurampelly, 2018). The transition events are categorized into three types to represent (a) intrachain, (b) interchain, and (c) the to and from polymer chain hopping events.

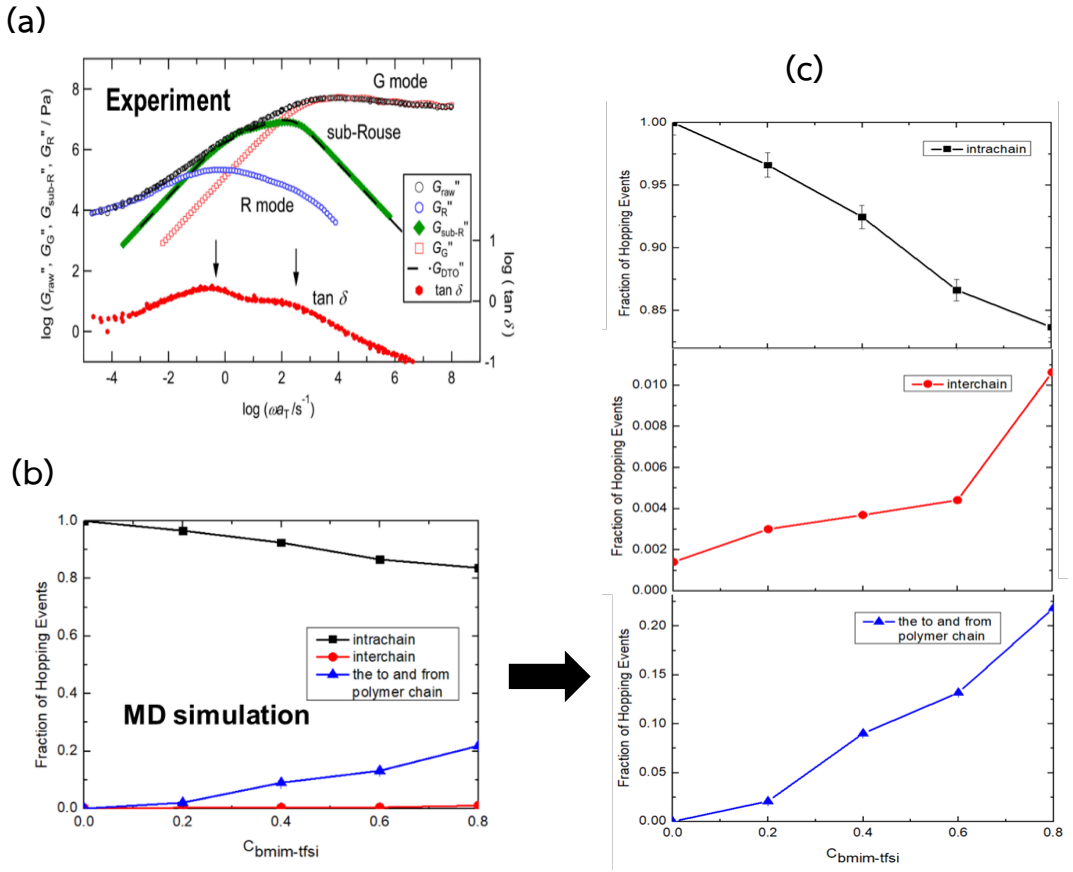

Figure 4.4.24 Fraction of transition rate of different hopping types as a function of pure ILs loading at 600K (a) Experimental result from (Inoue, 2013) (b) Result from MD simulation and (c) Individual result from MD simulation.